

Supernova explosions in active galactic nuclear discs

Evgeni Grishin^{1,3,4*}, Alexey Bobrick², Ryosuke Hirai^{3,4}, Ilya Mandel^{3,4,5}, Hagai B. Perets¹

¹Physics Department, Technion - Israel Institute of Technology, 3200003, Haifa, Israel

²Lund Observatory, Department of Astronomy and Theoretical Physics, Lund, Sweden

³Monash Centre for Astrophysics, School of Physics and Astronomy, Monash University, Clayton, Victoria 3800, Australia

⁴OzGrav: Australian Research Council Centre of Excellence for Gravitational Wave Discovery, Clayton, VIC 3800, Australia

⁵Institute of Gravitational Wave Astronomy and School of Physics and Astronomy, University of Birmingham, Birmingham, B15 2TT, United Kingdom

Accepted XXX. Received YYY; in original form ZZZ

ABSTRACT

Active galactic nuclei (AGN) are prominent environments for stellar capture, growth and formation. These environments may catalyze stellar mergers and explosive transients, such as thermonuclear and core-collapse supernovae (SNe). SN explosions in AGN discs generate strong shocks, leading to unique observable signatures. We develop an analytical model which follows the evolution of the shock propagating in the disc until it eventually breaks out. We derive the peak luminosity, bolometric lightcurve, and breakout time. The peak luminosities may exceed 10^{45} erg s⁻¹ and last from hours to days. The brightest explosions occur in regions of reduced density; either off-plane, or in discs around low-mass central black holes ($\sim 10^6 M_{\odot}$), or in starved subluminescent AGNs. Explosions in the latter two sites are easier to observe due to a reduced AGN background luminosity. We perform suites of 1D Lagrangian radiative hydrodynamics SNEC code simulations to validate our results and obtain the luminosity in different bands, and 2D axisymmetric Eulerian hydrodynamics code HORMONE simulations to study the morphology of the ejecta and its deviation from spherical symmetry. The observed signature is expected to be a bright blue, UV or X-ray flare on top of the AGN luminosity from the initial shock breakout, while the subsequent red part of the lightcurve will largely be unobservable. We estimate the upper limit for the total event rate to be $\mathcal{R} \lesssim 100 \text{ yr}^{-1} \text{ Gpc}^{-3}$ for optimal conditions and discuss the large uncertainties in this estimate. Future high-cadence transient searches may reveal these events. Some existing tidal disruption event candidates may originate from AGN supernovae.

Key words: galaxies: active – transients: supernovae – (stars:) supernovae: general – hydrodynamics – shock waves – (stars:) circumstellar matter

1 INTRODUCTION

The accretion discs of active galactic nuclei (AGN) are responsible for feeding supermassive black holes (SMBHs) in the centres of galaxies (Lynden-Bell 1969). These AGN discs are often described as geometrically thin and optically thick accretion discs, driven by the α -viscosity (Shakura & Sunyaev 1973). The rapidly growing observational data on AGN discs has led to more detailed models of their structure and evolution, either based on the mass flow inferred from star formation (Thompson et al. 2005), or on the optical/UV spectral energy distribution (SED) (Sirko & Goodman 2003).

Galactic nuclei also possess a large number of stars and stellar remnants (Miralda-Escudé & Gould 2000; Bartko et al. 2010). Some regions of the discs might become unstable and give rise to vigorous star-formation (Paczynski 1978; Dittmann & Miller 2020), and the interactions of stars and compact objects with the discs could lead to their capture and embedding into the discs (Artymowicz et al. 1993). Stars and compact objects in a gaseous environment could accrete gas and grow over time (Davies & Lin 2020; Cantiello et al. 2020), as well as change their orbits due to the interaction with the disc (Ostriker

1983; Syer et al. 1991; Artymowicz et al. 1993). The higher stellar density in the disc, the presence of gas, and the low relative velocities may enhance the formation of binaries through tidal effects (Cheng & Wang 1999) and/or through gas-mediated capture (Goldreich et al. 2002; Tagawa et al. 2020). The interactions of binary stars with the gaseous environment could catalyze stellar mergers (Baruteau et al. 2011), and the formation and gravitational-wave driven mergers of compact-object binaries (McKernan et al. 2012).

Taken together, AGN disc environments could potentially increase the rate of SNe, such as core-collapse SNe or type Ia SNe. The rate of core-collapse SNe may be increased through potentially increased formation rate of massive stars (Artymowicz et al. 1993). Similarly, the rate of type Ia SNe may be increased through an increased number of white-dwarf (WD) mergers (McKernan et al. 2020), or through accretion onto WDs, which can make them reach close-to-Chandrasekhar masses and explode (Ostriker 1983). Other explosive mergers of compact objects with stars or planets could give rise to other transients such as micro - tidal disruption events (when the stars are disrupted by such compact objects, Perets et al. 2016).

SNe in AGNs were studied in the context of the feedback on the AGN structure and evolution (Rozyczka et al. 1995; Ferrara & Tolstoy 2000; Moranchel-Basurto et al. 2021). Here we focus on the

* E-mail: eugeneg@campus.technion.ac.il (EG)

observational signatures of SN explosions in AGN discs. The highly relativistic electromagnetic signatures of γ -ray bursts (GRBs) and the accretion induced collapse of neutron stars (NS) into BHs have been recently explored (Zhu et al. 2020, 2021a; Perna et al. 2021b,a). Recently, Zhu et al. (2021b) suggested that type Ia supernovae may potentially be observable in AGN discs. However, a detailed model for the interaction of a non-relativistic SN explosion with the AGN disc and its observational signatures is still lacking. In this paper, we take the first steps in the detailed modelling of general SN explosions in AGN environments.

Electromagnetic signatures from the interaction between SN ejecta and the dense circumstellar medium (CSM) have been studied intensively in the context of type II SNs both analytically and numerically (e.g. Woosley et al. 2007; Chevalier & Irwin 2011; Ginzburg & Balberg 2012; Moriya et al. 2013; Dessart et al. 2015; Tsuna et al. 2019; Takei & Shigeyama 2020; Suzuki et al. 2021). Most studies assume a wind-like dense CSM, which has density profiles following $\rho \propto 1/r^2$, where r is the distance from the progenitor. Some studies have also dealt with asymmetrical CSM structures, such as disc-like morphologies (Suzuki et al. 2019). In all cases, the main feature is that the presence of the CSM allows the kinetic energy of the ejecta to be efficiently dissipated and converted into radiation, increasing the luminosity of these events. CSM interaction is considered to be the dominant channel for producing SNe with narrow-line features (type II_n) and the extremely bright SNe called superluminous SNe (SLSNe; see Gal-Yam 2019, for a review on SLSNe).

1.1 SNe in AGN discs

Motivated by the recent success of CSM interaction models in explaining SLSNe, we develop a detailed model for the shock propagation and breakout of an SN explosion inside an AGN disc. However, there are two main differences between the wind-driven CSM SNe and our setting. While the origin of the CSM in CSM SN is the wind itself, which is already expanding prior to the explosion (Nakar & Piro 2014; Morozova et al. 2017; Piro et al. 2020), in our case, the local AGN gas may be assumed to be static at the time of the explosion. The second difference is that the spatial extent of AGN discs overwhelmingly exceeds the distance scales of wind-driven explosions. For this reason, as we show further, explosions in an AGN disc can be analogous to explosions close to the surface of a much more massive ball of gas (Yalinewich & Matzner 2019).

The purpose of this paper is to describe the details of SN explosions in dense environments, such as AGN discs. Here we provide an intuitive picture of the underlying physical mechanisms and key takeaway messages.

After the explosion, a shock wave is generated and propagates outward. Initially, the shock propagation velocity is much faster than the photon diffusion speed in an optically thick environment. As the shock propagates outward, the medium outside it becomes increasingly optically thin, until the photons are able to overcome the shock velocity, break out before the shock and diffuse to the photosphere. This is the breakout shell z_{bo} , formally defined as a solution to the equation $\tau(z_{\text{bo}}) = c/v(z_{\text{bo}})$, where $v(z_{\text{bo}})$ is the shock velocity and $\tau(z_{\text{bo}})$ is the optical depth, all evaluated at z_{bo} . At this point, there is a surge of photons that escape out of the material, causing a sudden rise in the observable luminosity. After the initial breakout, the photosphere starts to expand and cool down, which will decrease the luminosity over time.

1.2 Overview and structure of the paper

The details of the shock propagation velocity and the breakout depend on the structure of the medium. In sec. 2, we review the structure and properties of AGN discs and derive the vertical density profile $\rho(z)$ and the optical depth $\tau(z)$. In sec. 3, we discuss our assumptions in 3.1, derive and compare the velocity profile $v(z)$ with numerical simulations in sec. 3.2. Once $v(z)$ is established, we find the breakout shell z_{bo} and the breakout time in sec. 3.3. The shock velocity depends on $\rho(z)$ and $\tau(z)$, and also on the spatial location, and internal properties of the explosion, namely the explosion energy E_0 and the ejecta mass M_{ej} .

Once the breakout shell z_{bo} and the photosphere z_{ph} (defined by $\tau(z_{\text{ph}}) = 1$) are established, the photon diffusion length scale is $d = z_{\text{ph}} - z_{\text{bo}}$. Since the velocity $v(z_{\text{bo}})$ is also known, we can estimate the peak luminosity L_{peak} as the energy deposited onto the breakout shell $e_{\text{bo}} \sim \rho(z_{\text{bo}})z_{\text{bo}}^2 dv_{\text{bo}}^2$ divided by the diffusion photon time $\sim d/v_{\text{bo}}$. The luminosity is then

$$L_{\text{peak}} = C_L \rho(z_{\text{bo}}) z_{\text{bo}}^2 v_{\text{bo}}^3. \quad (1)$$

The dimensionless prefactor C_L depends on the geometry of the explosion.

The energy deposited in layers beneath the breakout slab cannot efficiently diffuse out, and the material, therefore, cools mostly through adiabatic expansion. Adiabatic cooling leads to a rapid decay of the lightcurve: Initially, the volume is only linearly proportional with time $V \propto t$, and for a pressure P , the change in the energy will be $\int dE = \int P dV \propto \int V^{-\gamma} dV$. For a radiation dominated medium (which is the case after it is shocked), we have $\gamma = 4/3$, and $\int dE \propto V^{-1/3} \propto t^{-1/3}$, where we used the connection $PV^\gamma = \text{const}$. The luminosity falls off as $L \propto E/t \propto t^{-4/3}$. The peak luminosity is hence dominated by the initial breakout, which is likely to be the detectable portion of the lightcurve in the luminous environment of an AGN. In dense regions where the CSM mass until the breakout is much larger than the ejecta mass $M_{\text{CSM}} \gg M_{\text{ej}}$, adiabatic cooling is the main source of energy loss, while for models with lighter masses $M_{\text{CSM}} \lesssim M_{\text{ej}}$ the optical depth is reduced, and radiative losses will also contribute, and the decay will be steeper.

After some time, the photosphere will expand further out, the volume will expand spherically, the optical depth will decrease, and deeper layers will be exposed, which makes the lightcurve decay with a much shallower slope. Nakar & Sari (2010) found a slope of ≈ -0.35 for a radiative atmosphere profile.

The uncertainty of the peak luminosity in terms of the coefficient C_L and the complex structure make it difficult to predict the peak luminosity and subsequent lightcurve. Recent detailed modelling of explosions close to a stellar surface has provided analytical expressions which were corroborated numerically (YM19). We extend the modelling of YM19 to apply it to our disc geometry under certain approximations in sec. 3.4 and derive an approximate analytic expression for the lightcurves in sec. 3.5.

In sec. 4, we present the different initial conditions for our models, which include different internal properties and spatial locations for the explosions, different vertical profiles and SMBH masses, as well as discs with reduced densities. We also describe the numerical techniques used in this paper. We devote sec. 5 to describing the obtained lightcurves for the aforementioned models, both analytically and numerically. We discuss which models are in good agreement between the analytic and numerical models, and which differ and why.

Finally, we discuss the observational aspects of our results in sec. 6. We discuss which of the events may be observable and could be distinguished from the underlying AGN luminosity. We then estimate

the total rates of these events, their observed fraction and the origins of their large uncertainty. We also briefly discuss the response of the disc and comment on AGN variability and potential past and future observations of SNe explosions in AGNs.

We make a summary of our key points in sec. 7. Readers interested in the key takeaway messages without the technical details can directly skip to this section.

2 AGN DISC STRUCTURE AND PROPERTIES

AGN discs are powered by accretion and are expected to be geometrically thin but optically thick (although there may be optically thin windows, see sec. 2.3). In order to describe AGN disc structures, we use several parameters. The radial coordinate r is expressed in units of the Schwarzschild radius $r_s \equiv 2GM_\bullet/c^2 \approx 1.974M_8 \text{ AU}$, where $M_8 \equiv M_\bullet/10^8 M_\odot$ is the SMBH mass normalized to $10^8 M_\odot$. The vertical structure is governed by the scale height H which is generally small compared to the size of the disc ($H \ll r$).

2.1 Radial structure models

AGN discs are generally modelled as viscous accretion discs. On the largest, galactic scales, discs are expected to be cold, gravitationally unstable and fragment into stars, with the effective Toomre $Q \equiv c_s \Omega / \pi G \Sigma \ll 1$, where c_s is the sound speed, Ω is the orbital frequency and Σ is the surface density. However, only a fraction of the gas is fragmented and the remaining gaseous component is still retained. The transition from the unstable galactic discs to accretion discs around a central object is still unclear. Angular momentum transport via global torques, rather than local viscosity, may keep the disc marginally stable and avoid fragmentation, which is the mechanism that is assumed in the [Thompson et al. \(2005\)](#) model throughout the disc, even at smaller radii.

The structure of AGN discs can be inferred from the optical/UV spectral energy distribution (SED) in the inner regions, and from mass inflow and star formation in the outer regions. [Sirko & Goodman \(2003, hereafter SG03\)](#) obtained an accretion disc model that fits the SED observations, while [Thompson et al. \(2005\)](#) constructed a model regulated by mass inflow and star formation. The SG03 model best describes the disc structure in the inner regions, up to $\lesssim 10^5 r_s$, which is the radial region of interest in our study

The radial gas density structure of the SG03 model may be inferred from the marginal gravitational instability condition (Eq. 15 of [SG03](#)),

$$\rho(r) = \frac{\Omega^2}{2\pi G Q_{\min}} \approx 1.22 \cdot 10^{-9} M_8^{-2} \left(\frac{r}{10^3 r_s} \right)^{-3} \text{ g cm}^{-3}. \quad (2)$$

The latter equation is valid for $r \geq 10^3 r_s$, where $Q_{\min} \approx 1$ in the SG03 model. The disc is expected to be dominated by radiation pressure $p_{\text{rad}} = aT^4/3$, where $a = 4\sigma_{\text{SB}}/c$ is the radiation constant and σ_{SB} is the Stefan-Boltzmann constant. In the SG03 model, radiation pressure indeed dominates in most parts of the disc. However, the gas pressure may have a significant contribution to the total pressure near $r \approx 10^3 r_s$. Nevertheless, we use the radiation pressure throughout the paper, and the adjustments needed to include other sources of pressure are straightforward.

The aspect ratio of a thin disc should be small, i.e. $H/r \ll 1$. In the SG03 model, the aspect ratio is approximately given by

$$\frac{H}{r} = 8 \cdot 10^{-3} \left(\frac{r}{10^3 r_s} \right)^{1/2}, \quad (3)$$

in our range of interest.

2.2 Vertical structure models

The vertical structure of an AGN disc and its stability are also under debate (see the review of [Davis & Tchekhovskoy 2020](#) for discussion and further references). While gas pressure dominated discs are expected to be vertically stable, the stability of radiation dominated discs is undecided. Theory predicts that radiation dominated discs will be unstable ([Shakura & Sunyaev 1976](#)). Contrary to this prediction, early radiative magneto-hydrodynamical (MHD) shearing box simulations, such as those with the ZEUS code, found that the disc is stable over many thermal timescales ([Hirose et al. 2009](#)). However, these results were later challenged by simulations with the ATHENA code. Although small box sizes reproduced the stability of [Hirose et al. \(2009\)](#), larger box size simulations resulted in an eventual runaway (where the disc either expands or collapses), although on much longer timescales than the thermal timescale ([Jiang et al. 2013](#)). Iron bound-bound opacity may revert the situation again and make the vertical structure stable around temperatures of $1.8 \cdot 10^5 \text{ K}$ ([Jiang et al. 2016](#)).

Given the uncertainties involved in the stability and the detailed vertical structure, we will remain agnostic about the true structure. Nevertheless, a different vertical structure can lead to different observational signatures for the same initial conditions of the explosion. Here we consider several possible models for the vertical structure as described below, where their main common feature is that they all describe a thin disc. Thus the vertical density profile should fall off sharply where the vertical height h is larger than the scale-height, $h \gtrsim H$. Note that it is rather different from a $\rho \propto r^{-2}$ distribution that is often assumed in studies of interaction-powered SNe. For our canonical model, we assume a Gaussian density profile

$$\rho_{\text{gas}}(h) = \rho_0 \exp\left(-\frac{h^2}{2H^2}\right); \quad \frac{z}{h} \in \mathbb{R}, \quad (4)$$

which is applicable for gas-dominated discs and is stable. We use hydrostatic equilibrium to derive the density profile for radiation dominated discs (if they are stable) in Appendix A,

$$\rho_{\text{rad}}(h) = \rho_0 \left(1 - \frac{h^2}{6H^2}\right)^3; \quad \left|\frac{h}{H}\right| < \sqrt{6}, \quad (5)$$

and present some of the results with this structure, as well as a simplified step profile of constant $\rho_{\text{step}} = \rho_0$ up to a scale height H away from the midplane. We assume that the disc is stable and static with the respective vertical structure prior to the explosion. We compare the results for different vertical structures in sec. 5.3.

2.3 Opacity

At high temperatures, $T > 10^4 \text{ K}$, the gas is mostly ionized and the opacity is dominated by electron scattering and bremsstrahlung (free-free). A typical value of the opacity in this range can be the electron scattering opacity $\kappa_{\text{es}} = 0.2(1+X) \text{ cm}^2 \text{ g}^{-1}$ where X is the Hydrogen fraction. The opacities may be enhanced by ≈ 2 orders of magnitude when detailed opacity tables are considered ([Iglesias & Rogers 1996](#), see also Fig. 3 of [Davis & Tchekhovskoy 2020](#)). At temperatures below $\sim 100 \text{ K}$, dust absorption is the dominant effect that increases opacity, which scales as $\kappa_{\text{dust}} \approx 2.4(T/100\text{K})^2 \text{ cm}^2 \text{ g}^{-1}$, while the opacity is roughly constant for $T \approx 10^2 - 10^3 \text{ K}$ in the range of $\kappa \approx 1 - 10 \text{ cm}^2 \text{ g}^{-1}$ (see Fig 1. of [Thompson et al. 2005](#), which is based on more recent opacity models of [Semenov et al. 2003](#)). For intermediate

temperatures around $10^3 - 10^4$ K, the gas is neutral, and most of the dust is already sublimated, thus the opacity is extremely low. Depending on the radial temperature profile, an optically thin window is expected to occur in AGN discs. The discs are optically thin at $r \gtrsim 10^4 r_s$ in the models we adopted. Explosions in the optically thin region will look like standard SNe as the emitted radiation will be unaffected by the surrounding disc, while the associated kinetic outflows will be choked by the enormous mass. Explosions in the optically thick and massive regions ($\approx 10^4 r_s$ for $M_\bullet = 10^7 M_\odot$) will be completely choked (see sections 4 and 6). For our analytical modeling, we use a constant electron scattering opacity of solar composition ($X = 0.7$), $\kappa_{\text{es}} = 0.34 \text{ cm}^2 \text{ g}^{-1}$. We use realistic OPAL tables (Iglesias & Rogers 1996) for our radiative transfer simulations (see sec. 4 for details).

2.4 Optical depth

For a constant opacity κ , the optical depth at height h , in the direction normal to the disc, is given by

$$\tau(h) = \kappa \int_h^\infty \rho(h') dh' \equiv \tau_0 \mathcal{F}(\zeta), \quad (6)$$

where we defined for convenience the dimensionless quantities $\tau_0 \equiv \kappa \rho_0 H$, and $\zeta \equiv h/H$. The functional form of $\mathcal{F}(\zeta)$ depends on the vertical structure.

For a uniform step density, the integral is straightforward, and the solution is $\tau(h) = \kappa \rho_0 (H - h) = \tau_0 (1 - \zeta)$ for $0 \leq h \leq H$ and $\tau = 0$ for $h > H$ since there is no material there. This leads to $\mathcal{F}_{\text{step}}(\zeta) = 1 - \zeta$.

For the Gaussian profile, applicable for the gas dominated disc, we have

$$\mathcal{F}_{\text{gas}}(\zeta) = \frac{1}{H} \int_h^\infty \exp\left(\frac{-h'^2}{2H^2}\right) dh' = \sqrt{\frac{\pi}{2}} \operatorname{erfc}\left(\frac{\zeta}{\sqrt{2}}\right) \quad (7)$$

where $\operatorname{erfc}(x)$ is the complimentary error function.

For the radiation-dominated profile, we have

$$\mathcal{F}_{\text{rad}}(\zeta) = \frac{1}{H} \int_h^{\sqrt{6}H} \left(1 - \frac{h'^2}{6H^2}\right)^3 dh' = \int_\zeta^{\sqrt{6}} \left(1 - \frac{\zeta'^2}{6}\right)^3 d\zeta' = p(\zeta), \quad (8)$$

where $p(\zeta) = 16\sqrt{6}/35 - \zeta + \zeta^3/6 - \zeta^5/60 + \zeta^7/1512$.

3 ANALYTIC LIGHTCURVE MODELING

Here we model the lightcurve of typical explosions. We first discuss the assumptions of the model. We then proceed to discuss the velocity of the shock front, and finally calculate the the lightcurve by drawing analogies between our disc explosions and the recently developed theory of surface explosions. Although our analysis is generic, when applicable, we refer to our canonical model (1) of an explosion of energy $E_0 = 10^{51}$ erg and ejecta mass $M_{\text{ej}} = 1.3 M_\odot$, which serves as a proxy for a standard type Ia SN explosion. The radial location of the explosion is at $r = 10^3 r_s$ around an SMBH of mass $10^7 M_\odot$, in the disc midplane. The disc has density $\rho_0 = 1.22 \cdot 10^{-7} \text{ g cm}^{-3}$ and scale height $H = 8 \cdot 10^{-3} r = 2.36 \cdot 10^{13} \text{ cm}$ with a gas-dominated Gaussian vertical profile. For the opacity, we make use of a constant opacity

$\kappa = 0.34 \text{ cm}^2 \text{ g}^{-1}$, which corresponds to electron scattering at Solar compositions. The optical depth is then $\tau = \sqrt{\pi/2} \kappa \rho_0 H = 1.2 \cdot 10^6$. Other models are described in sec. 4 and their initial conditions are summarized in table 1.

3.1 Assumptions

Here we describe the assumptions made in constructing our solution for shock propagation, breakout and the resulting lightcurve. Consider an explosion going off in dense material. If the material is sufficiently optically thick and the prompt energy deposition is sufficiently energetic, the primary mode of energy transport, at least initially, will be kinetic outflows rather than radiation transport (photon diffusion). The initial disc temperature is T_0 , and the explosion is spherical. For collimated outflows, not considered here, one would need to introduce an additional solid angle Ω_s , spanned by the outflow.

i) Is the outflow relativistic? The characteristic velocity of a non-relativistic outflow is $v_0 = \sqrt{E_0/M_{\text{ej}}}$, so we require that $(v_0/c)^2 = E_0/(M_{\text{ej}}c^2) \ll 1$ for an outflow to be non-relativistic. And indeed, for the canonical model, representative of type Ia SNe, $v_0/c = 0.02$. Similarly, core-collapse SNe also produce non-relativistic outflows.

ii) Is the kinetic outflow the dominant form of energy transport? For this, the velocity must be faster than the photon diffusion speed, at least initially, or, equivalently, the depth must be sufficiently large. The optical depth at height z is formally given by Eq. 6. If at the explosion site the local density is ρ_0 and the shock propagates over a typical distance, R_0 , the optical depth is approximately estimated as $\tau \sim \kappa \rho_0 R_0$, where κ is the opacity, and the diffusion speed is c/τ . For kinetic outflow to dominate, we require $v_0 \gg c/\tau$, or $\tau^2 E_0/M_{\text{ej}}c^2 \gg 1$. Combining conditions *i)* and *ii)*, the optical depth must also be large, $\tau \gg 1$. Note that this defines a hierarchy of velocities $c/\tau \ll v_0 \ll c$. For our canonical model, the explosion is at the midplane, and the midplane optical depth ($z = 0$) is estimated as $\tau \gtrsim 10^6$, so these conditions are initially satisfied.

iii) Does the shock leave radiation-dominated material behind? To answer this question, we require that the radiation energy density aT^4 , which may be approximated by $\sim \rho v_0^2$ near shock, will be much larger than the gas energy density $\rho k_B T/m_p$, where k_B is Boltzmann's constant and m_p is the proton mass. Eliminating the temperature, this condition becomes equivalent to $(\rho v_0^2/a) \gg (k_B \rho/m_p a)^{4/3}$, or

$$v_0^2 = \frac{E_0}{M_{\text{ej}}} \gg \left(\frac{k_B^4 \rho}{m_p^4 a}\right)^{1/3}. \quad (9)$$

The latter is only an estimate within an order of magnitude.

Note that the latter three conditions are equivalent to the assumptions made by Yalinewich & Matzner (2019, hereafter: YM19) in the context of surface explosions. We return to the detailed modeling of YM19 in our lightcurve modelling in sections 3.4-3.5.

3.2 Shock velocity profile

Here we discuss several models for the shock velocity profile. The description is mostly generic, although sometimes, for a concrete example, we use the canonical model (model (1) in table 1). We later investigate how the variation of some of the disc and explosion properties affect our results in sec. 5.

For an explosion with energy E_0 and ejecta mass M_{ej} , the typical velocity is $v_0 \equiv \sqrt{E_0/M_{\text{ej}}}$. The outflow in the plane of the disc will be quenched by the disc material, and the shock will break

out in the vertical direction. Therefore, we focus on the vertical height z above the explosion. Generally speaking, a shock wave is always accompanied by three waves: forward shock, reverse shock (or rarefaction), and the contact discontinuity. In our context, the forward shock compresses the CSM, while the reverse shock compresses the ejecta. The contact discontinuity separates the ejecta and the CSM matter. For most of our models, the CSM matter is more massive than the ejecta, so the reverse shock quickly traverses the ejecta while the forward shock is still propagating outwards. We therefore focus only on the forward shock, unless stated otherwise explicitly.

The shock velocity will depend on the shock front radius $z(t)$ and on the density at this radius. Generally, three qualitatively different regimes will be evident:

i) Free expansion regime: In this case, the swept mass $M(z)$ is much smaller than the ejected mass, i.e., $M(z) \sim \rho(z_{\min})(z(t) - z_{\min})^3 \ll M_{\text{ej}}$, where z_{\min} is the vertical location of the explosion site, $z(t)$ is the height reached by the shock at time t , and the shock velocity is close to v_0 . *ii) Sedov-Taylor deceleration regime:* Once the swept mass becomes comparable to the ejecta mass, $M(z) \gtrsim M_{\text{ej}}$ the shock front will decelerate. Dimensional analysis leads us to a length scale $z(t) = \beta(E_0/\rho(z_{\min}))^{1/5}t^{2/5}$ and a velocity scale

$$v_{\text{ST}}(t) = \frac{dz}{dt} = \frac{2\beta}{5} \left(\frac{E_0}{\rho(z_{\min})} \right)^{1/5} t^{-3/5}. \quad (10)$$

Here, β is an order unity parameter which can in principle be estimated from the energy equation. We take for simplicity $\beta = 1$. The latter scaling is the self-similar Sedov-Taylor (ST) solution (Sedov 1946; Taylor 1950), where the shock front expands as $R \propto t^{2/5}$ and the shock velocity decelerates $v_{\text{ST}} \propto t^{-3/5}$.

iii) Sakurai accelerating regime: The ST picture is correct if the density is uniform. The vertical structure of the disc is generally far from uniform. Close to the disc edge (either the physical edge or the photosphere, if the disc is formally infinite), the density gradient is quite steep, and the shock propagates more easily, which causes it to accelerate with decreasing density as $v \propto \rho^{-\mu}$, which is known as the Sakurai law (Sakurai 1960). For radiation dominated material, $\mu \approx 0.19$ fits well with previous estimates (see also Matzner & McKee 1999, hereafter MM99, their sec. 4.2 and references therein for more details and discussion). Note that the latter picture is valid if the swept mass $M(z) \gtrsim M_{\text{ej}}$. Some of our models have the swept mass comparable to or smaller than M_{ej} , and in these cases the ST phase is skipped and the shock may only accelerate or directly breakout.

Close to the centre, the density is almost constant, and the evolution is as in the ST regime. Close to the edge, a small change in the radial scale leads to a large change in the density, and therefore the shock will follow the Sakurai law. It is possible to write down a general formula that includes both cases, as done in MM99:

$$v(t) = v_0 \left(\frac{t_1}{t} \right)^{3/5} \left(\frac{\rho(z(t))}{\rho(z_{\min})} \right)^{-\mu}, \quad (11)$$

where t_1 is the time when a transition from the free expansion to the ST deceleration occurs and is given by $v_{\text{ST}}(t_1) = v_0$ from Eq. 10. Plugging t_1 into the ST length scale leads to $z(t_1) = z_1 = (4M_{\text{ej}}/25\rho(z_{\min}))^{1/3}$. The transition occurs when the swept mass is $4M_{\text{ej}}/25 = 0.16M_{\text{ej}}$. For the ejecta mass of $1.3M_{\odot}$, as in our model 1, the transition occurs at $0.21M_{\odot}$, or at radius $z \approx 1.5 \cdot 10^{13}$ cm = $0.63H$.

The transition from the ST decelerating velocity to Sakurai accelerating velocity occurs when $v(t)$ is at a minimum. From the ST solution, we can invert $z(t)$ to $t(z) \propto z^{5/2}$ and find the location of

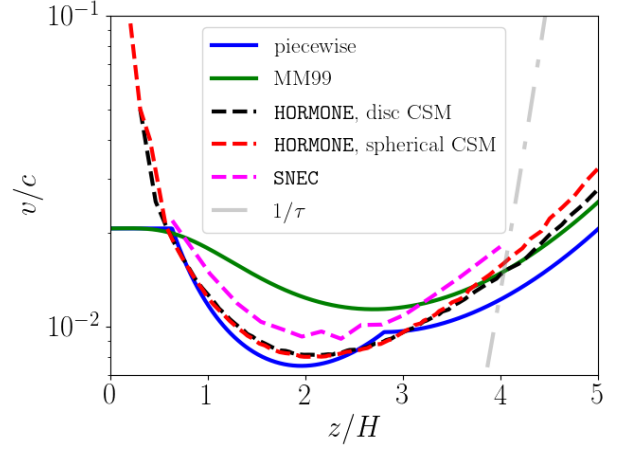


Figure 1. Shock velocity prescriptions for model 1 in the AGN disc, in units of the speed of light c . The solid lines are the theoretical shock velocities; the piecewise model (blue), Eq. (12), and the MM99 model (green), Eq. (13). The dashed lines are the numerical shock velocities. The hydrodynamical code HORMONE is used to obtain the matter velocity v_m just behind the shocked CSM, and the shock velocity is $v_m(\gamma + 1)/2$ in the disc geometry (dashed black) and spherical geometry (dashed red). The result from the spherically-symmetric radiative transfer code SNEC is also presented in magenta. For completeness, the photon diffusion velocity, which is also the inverse of the optical depth, is shown in dot-dashed grey lines. The shock breakout occurs when the gray line crosses the shock velocity, which occurs close to $z \sim 4H$ for all shock velocity estimates for model 1.

the minimum z_2 given by $d \ln \rho / d \ln z|_{z_2} = -3/(2\mu)$. For a Gaussian profile, the velocity behaves as $v \propto z^{-3/2} \exp(\mu z^2/(2H^2))$, the logarithmic derivative of the density is $d \ln \rho / d \ln z = -(z/H)^2$, and the minimum is achieved at $z_2/H = (3/(2\mu))^{1/2} \approx 2.8$.

The three regimes and their transitions described above allow us to construct two possible solutions. The first is the piecewise velocity solution. Here we divide the behaviour into three regimes, where we first begin with free expansion and transform to ST deceleration. The ST approach is not accurate since it was developed for a uniform density. The density change is negligible for $z \ll H$, but it is already significant at z_1 . We use an effective scaling where we replace $\rho(z_{\min})$ in the ST solution by $\rho(z)$. Although not entirely self-consistent, we can write v as in Eq. (11) but with an effective density power law $\mu' = \mu + 1/5$, where the $1/5$ is coming from the ST scaling of $z \propto \rho^{-1/5}$. The piecewise velocity is

$$v_p(z) = v_0 \begin{cases} 1 & z < z_1 \\ \left(\frac{z_1}{z} \right)^{3/2} \left[\frac{\rho(z)}{\rho_1} \right]^{-(\mu+1/5)} & z_1 < z < z_2 \\ \left(\frac{z_1}{z} \right)^{3/2} \left(\frac{\rho_2}{\rho_1} \right)^{-(\mu+1/5)} \left[\frac{\rho(z)}{\rho_2} \right]^{-\mu} & z > z_2 \end{cases} \quad (12)$$

where $\rho_i = \rho(z_i)$ for $i = 1, 2$.

Another solution is the direct MM99 shock velocity

$$v_{\text{MM99}}(z) = \left(\frac{E_0}{M_{\text{ej}} + M(z)} \right)^{1/2} \left(\frac{\rho(z)}{\rho(z_{\min})} \right)^{-\mu}, \quad (13)$$

Note that Eq. (13) captures well all of the regimes. For $M_{\text{ej}} \gg M(z)$ the density and hence the velocity are essentially constant. When $M(z) \gg M_{\text{ej}}$ but $\rho(z) \sim \rho(z_{\min})$, the velocity is $\propto z^{-3/2} \propto t^{-3/5}$ as expected from a ST solution. Finally, once $\rho(z) \ll \rho(z_{\min})$, the Sakurai term dominates the acceleration.

Figure 1 shows the different velocity models for the canonical (model 1) explosion together with the shock velocity obtained numerically. The detailed description of the hydrodynamical code HORMONE

and the radiative transfer code SNEC appears in sec. 4. The three velocity regimes are clearly evident. The flat free expansion phase lasts until $z_1/H \approx 0.63$ for model 1, where the velocity starts to decelerate. The transition to Sakurai acceleration occurs somewhere around $z/H \sim 2 - 2.8$. We see that the matter-derived shock velocity $v_m(\gamma + 1)/2$ better agrees with the piecewise model, while the SNEC shock velocity is somewhere in between the piecewise and MM99 model. In either case, the overall acceleration in the low-density outskirts of the disc is underestimated.

In summary, there are two main theoretical shock velocity estimates for an explosion inside the AGN disc: a piecewise fit explicitly taking account the three distinct propagation regimes (Eq. 12), and a direct continuous measure of the swept mass (MM99 - Eq. 13). The numerical shock velocity falls between the two theoretical shock velocity models.

3.3 Breakout time

Even though the shock is accelerating in the Sakurai regime, the photon diffusion velocity rises more steeply. Eventually, the photon diffusion speed $c/\tau(z)$ will intersect the shock velocity $v(z)$. The two velocities are equal when the grey dot-dashed line intersects the velocity model of choice in Fig. 1. The location of this intersection defines the breakout shell z_{bo} , which is implicitly given by $\tau(z_{\text{bo}}) = c/v(z_{\text{bo}})$ and is around $\sim 4H$ for model 1, regardless of the velocity model.

The breakout time t_{bo} is the time elapsed for the first light to be beyond the breakout shell from the time of the explosion. In order to finally escape, the photons need to diffuse up to the photosphere. This diffusion time is much shorter than the breakout time.

The breakout time can be calculated by

$$t_{\text{bo}} = \int_{z_{\text{min}}}^{z_{\text{bo}}} \frac{dz}{v(z)} \quad (14)$$

The exact expressions are given either by special functions or integrated numerically. We provide them in Appendix B, together with the expressions for off-plane explosions.

3.4 Modelling AGN explosions as surface explosions

Surface explosions are explosions that occur in a relatively sparse material, close to a surface of a medium and far away from the dense core of the medium (e.g. a massive star). YM19 studied in detail such surface explosion in massive stellar envelopes. Our explosion is analogous to a surface explosion in the following way. Due to the planar geometry of the disc and its large spatial extent $r \gg H$, an explosion in the midplane of the disc cannot propagate in the in-plane direction, and the breakout occurs effectively on the vertical surface of the disc. This is analogous to an explosion at a distance $l \ll R_*$ below the surface of a star, the model for which was recently put forward by YM19. The shock propagates only upwards. Here we parametrise our explosion as a surface explosion, with some limitations.

3.4.1 Choosing length scales

The YM19 model assumes that the density vanishes at some boundary z_b and that the density scales as a power law profile of the form $\rho = \rho_0(x/l)^\omega$ where x is the distance from the edge and l is a typical length scale of order the distance of the explosion hotspot from the

edge. When applied to our extended model, l is generally on the order of H , but its exact definition has some ambiguities as we discuss below.

The surface explosion modelling in YM19 is encapsulated by two dimensionless parameters, $\Gamma \equiv E_0/(c^2\rho_0 l^3)$ and $\tau_0 = \kappa\rho_0 l$. Initially, the only length scale we have is H . In YM19, l has several different roles:

- i) The distance from the explosion to the edge.
- ii) The transition between the end of the Sedov-Taylor phase and the beginning of the shock acceleration phase.
- iii) The value in the expression for the velocity at the end of the Sedov-Taylor phase, $v_{\text{ST}} = \sqrt{E_0/\rho_0 l^3}$.

These three definitions appear to be contradictory. First, the free expansion phase is ignored, or a point-source explosion is assumed. Second, after passing a length l (as in i.), formally, we should be at the edge, which is definitely after the breakout. However, according to ii. and iii., it is only the phase where the shock starts to accelerate and is assumed to be optically thick.

These differences are small in the stellar atmosphere with its steep density profile towards the edge. However, we saw that for model 1, the differences between the transition to accelerating shock at $z_2 = 2.81H$, the breakout shell at $z_{\text{bo}} = 3.99H$ for the piecewise model and $z_{\text{bo}} = 3.96H$ for the MM99 model, and the photosphere at $z_{\text{ph}} = 4.93H$, are around a scale height away from each other. Moreover, free expansion phase ends at $z_1 = 0.64H$, which is also comparable to the scale height.

The velocity at the end of the ST phase is $v_{\text{ST}} \sim c\Gamma^{1/2}$. Hence the effective length scale l_{eff} in this case should replicate the total range of the swept mass from the end of the free expansion phase until the breakout shell. We therefore set $l_{\text{eff}} = z_{\text{bo}} - z_1$, unless otherwise specified.

$$\Gamma = \frac{E_0}{c^2(M_{\text{ej}} + \rho_0 l_{\text{eff}}^3)}. \quad (15)$$

Here, the inclusion of M_{ej} in the denominator extends the analysis of YM19 to include the free expansion phase and also avoids unphysically large values of Γ for low densities or small l_{eff} .

The optical depth τ_0 should be comparable with the midplane optical depth, hence we keep τ_0 as $\kappa\rho_0 H$.

3.4.2 Effective power law index ω_{eff}

Once we set l_{eff} and Γ for the explosion and also have ρ_0, H and τ_0 from the AGN disc model, we can assign an effective power law index ω_{eff} in the following way: ω_{eff} is a local value and formally varies along the vertical shock propagation.

For a local density profile

$$\rho(x) = \rho_a(x/l_{\text{eff}})^{\omega_{\text{eff}}}, \quad (16)$$

where ρ_a is the density at a distance l_{eff} from the edge, and $0 \leq x \leq l_{\text{eff}}$ is measured from the edge. We impose a matching condition on $d \ln \rho / dz$ between the assumed disc density profile and the power law model in order to fix ω :

$$\rho_a = \rho(z_{\text{ph}} - l_{\text{eff}}); \quad \omega = -l_{\text{eff}} \left. \frac{d \ln \rho}{dz} \right|_{z_{\text{ph}} - l_{\text{eff}}}. \quad (17)$$

For the slab profile, the derivative is zero and thus $\omega_{\text{eff}} = 0$ everywhere. For the Gaussian profile, $d \ln \rho / dz = -z/H^2$, and

$$\omega_{\text{gas}}(l_{\text{eff}}) = \frac{l_{\text{eff}}(z_{\text{ph}} - l_{\text{eff}})}{H^2}. \quad (18)$$

For the radiation dominated profile the power law is

$$\omega_{\text{rad}}(l_{\text{eff}}) = 6 \frac{\sqrt{6}H - l_{\text{eff}}}{2\sqrt{6}H - l_{\text{eff}}}, \quad (19)$$

where we used the actual edge of the disc $z_{\text{edge}} = \sqrt{6}H$ instead of the photosphere.

We note that ρ_a , l_{eff} and Γ are determined by the extent of the mass swept by the outflow prior to the breakout. τ_0 is also well defined. Although Eq. 17 suggests that determining l_{eff} uniquely determines ω_{eff} , this is misleading, since in the YM19 model of Eq. (16), the density profile is a global power with index ω_{eff} , while in our case the power law is only a local fit to the density profile. Therefore, we have the freedom to decide where to match the density profile to the power law. We opted to do so at the depth of l_{eff} beneath the breakout shell in equations 18 and 19. We could alternatively choose to do so at the breakout radius z_{bo} in an attempt to model the immediate post-breakout behavior more accurately; we consider this alternative choice in section 5.4. Regardless of the local choice of ω_{eff} , the dependence of the luminosity on ω is expected to be much weaker than on the other parameters.

3.5 Lightcurves

As mentioned in 1.2, the slab geometry leads to adiabatic expansion in the optically thick regime and rapid decay. The setting is similar to an explosion close to a stellar surface studied by YM19. They applied the latter arguments for a surface explosion using the dimensionless parameters Γ and τ_0 as discussed in sec. 3.4, where an additional phase, where the hotspot of the explosion becomes optically thin enough, which allows depletion of material deeper than the hotspot and forming a crater. The time of the transition where the hotspot is exposed is found to be $t_{\text{sph}} = (H/c)\tau_0^{1/2}\Gamma^{-1/4}$ (Eq. 24 of YM19).

Once we find l_{eff} , ω_{eff} , followed by Γ and τ_0 as describe in sec. 3.4, we can use YM19's modelling for the lightcurve. From now until the end of the section, we drop the 'eff' subscript and simply write ω to avoid cumbersome notation. The resulting luminosity is

$$\frac{L(t)}{E_0 c/H} = \begin{cases} \Gamma^{(\omega\mu-2\omega/3-5/6)\delta_-} \tau_0^{(5\omega\mu/3-\omega-4/3)\delta_-} \left(\frac{ct}{H}\right)^{-4/3} & \text{pl} \\ \Gamma^{(-\omega\mu+1/6)\delta_+} \tau_0^{(\omega\mu/3-\omega-4/3)\delta_+} \left(\frac{ct}{H}\right)^{(-4\omega\mu+2/3)\delta_+} & \text{sph} \end{cases} \quad (20)$$

in the planar and spherical phases, respectively, where $\delta_{\pm} \equiv (1 \pm \omega\mu + \omega)^{-1}$. For concreteness, we choose $\omega(l_{\text{eff}})$ as in equations 18 and 19.

In certain cases, we will use an expansion of ω_{eff} close to the edge, where we use $\omega_{\text{eff}}^{\text{edge}} = \omega_{\text{eff}}(l_{\text{edge}})$ with $l_{\text{edge}} = z_{\text{edge}} - z_{\text{bo}}$, where the edge is either the physical edge of the disc (for radiative and slab models), or the photosphere (for Gaussian models). We discuss this choice and its implications in the results section.

Fig. 2 shows the analytic lightcurve for model 1 in solid blue and the numerical SNEC lightcurve in dashed red. We shifted the analytical curve in time so that the breakout falls on top of the maximal luminosity of the numerical curve. After the peak, SNEC model luminosity is initially more shallow than the $L \propto t^{-4/3}$ decay expected in the planar phase from the simple arguments of section 1.2, but subsequently steepens before becoming more shallow again at the transition to the spherical phase. After the initial breakout with $L \sim 10^{44}$ erg s⁻¹, the luminosity rapidly decays by one order of magnitude over ~ 0.4 d from breakout and then decays more shallowly during the spherical phase. The end of the spherical phase

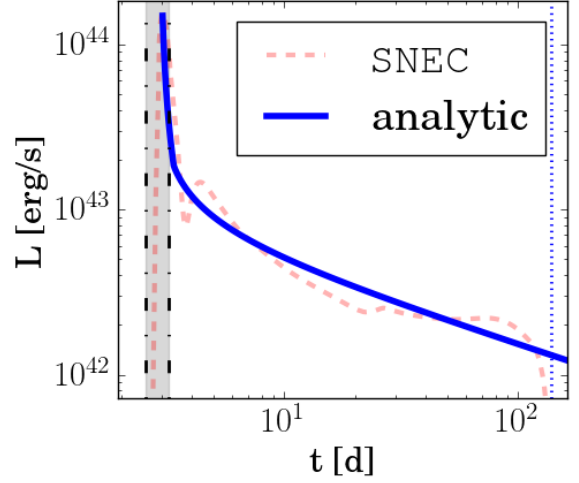


Figure 2. Analytical lightcurve for model 1. We show the analytic bolometric luminosity (i.e. the lightcurve) as a function of time with the solid blue curve. The numerical SNEC result is shown as a dashed red curve. The analytic curve is the maximum of the planar and spherical phases in Eq. 20. The vertical dot-dashed lines are the breakout times for the two velocity models given in Eq. B1 and B2, where the rightmost one is for the piecewise model since it has a lower velocity than the MM99 model. The gray area between them is the expected range of the breakout times. The dotted blue vertical line is the end of the spherical expansion phase, t_{sph} .

is indicated by the dotted vertical line around ~ 150 d. The gray area in the region between $t_{\text{bo}}|_{\text{MM99}} < t < t_{\text{bo}}|_{\text{pw}}$ is given by Eqs. B2 and B1, respectively, and indicates the range of times when the breakout occurs. In addition, the SNEC lightcurve is also plotted in dashed red, where the peak luminosity of the analytic model is set to match the peak luminosity of the SNEC lightcurve, which falls in the margins of the breakout time. Overall, there is a good correspondence, and the bumps in the SNEC lightcurve can be attributed to the reverse shock initially and varying opacity effects at later times, as discussed in detail in section 5.

We note that in order to set z_{bo} (and then l_{eff} , ω , Γ and the lightcurve), we need to solve for the breakout shell $\tau(z_{\text{bo}}) = c/v_{\text{bo}}$. This is done numerically using the standard `fsolve` function of Python's `scipy.optimize` package. We also need to choose a model for the velocity. We use the earlier derived piecewise model, Eq. 12, since the numerical breakout time is close to the breakout time evaluated using this velocity prescription. We also tried the MM99 prescription, and it gave almost indistinguishable results in most cases.

4 NUMERICAL SIMULATIONS

Here we describe the numerical approach and initial conditions for our simulations and analysis.

4.1 Initial conditions

We already introduced the initial conditions for our baseline model at the beginning of section 3. In order to explore the sensitivity to other parameters of the disc and the explosion, we also studied several other models, varying one or two parameters at a time. For changes in the global disc structure with the SMBH mass, we adopt the following scalings from the SG03 model. At radial locations scaled by the

#	M_{\bullet}	r/r_s	E_{51}	$\rho(z)$	z/H	M_{CSM}/M_{\odot}	Remarks
1	10^7	10^3	1	Gas	0	12.8	a
2	10^7	10^4	1	Gas	0	390	b
3	10^8	10^3	1	Gas	0	128	c
4	10^6	10^4	1	Gas	0	39	b,c
5	10^7	10^3	10	Gas	0	12.8	d
6	10^7	10^3	0.1	Gas	0	12.8	d
7	10^7	10^3	1	Rad	0	7.6	e
8	10^7	10^3	1	Step	0	3.4	e
9	10^7	10^3	1	Gas	1	1.92	f
10	10^7	10^3	1	Gas	2	0.15	f
11	10^7	10^3	1	Rad	1	0.5	e,f
12	10^7	10^3	1	Rad	2	$6.4 \cdot 10^{-4}$	e,f
13	10^6	10^3	1	Gas	0	1.28	c
14	10^7	10^3	1	Gas	0	1.28	g
15	10^7	10^3	1	Gas	0	12.8	h

Table 1. Initial conditions for the simulations. The columns are: simulation number, central BH mass (in M_{\odot}), radial location, explosion energy (in 10^{51} erg), the vertical height above the midplane, CSM mass (Eq. 21), and remarks describing the parameters being varied: a) The canonical model. b) Model with varied radial distance r . c) Model with varied mass of the SMBH. d) Model with varied explosion energy E_0 . e) Model with varied vertical density profile $\rho(z)$. f) Model with varied vertical distance z . g) Model with a reduced density $\rho_0 = 1.23 \cdot 10^{-8}$ g cm $^{-3}$ to mimic a starved AGN. h) Model with a larger ejecta mass, $M_{\text{ej}} = 10M_{\odot}$, to mimic a core-collapse SN.

gravitational radius of the SMBH, i.e. at $r \propto r_s \propto M_{\bullet}$, the midplane density is $\rho \propto \Omega^2 \propto M_{\bullet}/r^3 \propto M_{\bullet}^{-2}$. The rescaled interacting mass is $\rho H^3 \propto M_{\bullet}$. The optical depth is also rescaled as $\tau \propto \rho H \propto M_{\bullet}^{-1}$. The aspect ratio is taken from Eq. 3.

Table 1 lists the grid of initial conditions for the numerical simulations. Model 1 is our baseline canonical model, representing a typical type Ia SN explosion. Models 2-4 and 13 explore the impact of the SMBH masses and the radial location. Models 5-6 explore the impact of the explosion energy. Models 7-8 and 11-12 explore the impact of the vertical profile. Models 9-12 explore the impact of the vertical location. Model 14 mimics a starved AGN disc with reduced density, while Model 15 mimics a core collapse SN by considering more massive ejecta than in other models, $M_{\text{ej}} = 10 M_{\odot}$. The explosion energy of SN 1987A is estimated at $(1.5 \pm 0.12) \times 10^{51}$ erg (Utrobin 2007). The observed explosion energies of core-collapse SNe range from a few times 10^{50} erg to $\sim 10^{53}$ erg for hypernovae with massive progenitors (Janka 2012). We therefore keep the explosion energy at 10^{51} erg for model 15 as most representative for core-collapse SNe.

The CSM mass in the penultimate column of table 1 is defined as

$$M_{\text{CSM}} = 4\pi \int_{z_{\min}}^{z_{\max}} \rho(z)(z - z_{\min})^2 dz, \quad (21)$$

which depends on the density profile, and the maximal and minimal vertical locations. In Eq. 21, we assumed a spherical approximation, namely that the most significant interaction of the ejecta with the disc

material will be in the vertical direction, allowing us to approximate the density profile at radius r as $\rho(r) = \rho(z = r)$. This is true in our geometry since the in-plane directions are choked. We perform the explicit calculation of the CSM mass for each model in Appendix C.

4.2 Spherically symmetric lightcurve modelling

To model the lightcurves arising from the CSM interaction numerically and verify our analytic models, we perform detailed simulations with the supernova explosion code SNEC (Morozova et al. 2015a,b). SNEC is a spherically-symmetric Lagrangian radiative-hydrodynamics code that accounts for shock propagation through the use of artificial viscosity. Compared to our analytic models, SNEC directly solves the equations of radiative hydrodynamics and, therefore, allows us to assess the validity of our approximations. Additionally, it allows us to gain some intuition into the importance of ionisation, detailed opacities and heating from ^{56}Ni for forming the final lightcurves.

SNEC uses OPAL opacities (Iglesias & Rogers 1996) in the high-temperature regime (at $3.75 < \log_{10} T/\text{K} < 8.7$) and the solar-scaled Ferguson et al. (2005) opacities, which accounts for molecular contributions, in the low-temperature regime (at $2.7 < \log_{10} T/\text{K} < 4.5$). In the overlapping regions, the low-temperature opacity is preferred. The code accounts for ionisation states by solving the equilibrium Saha equation and models radiative transfer through flux-limited equilibrium photon diffusion. SNEC also models the contribution to the lightcurve from the radioactive decay of ^{56}Ni and ^{56}Co . The decay leads to the deposition of gamma-rays and positrons, which heat the ejecta, with gamma-rays dominating the heat deposition. The code solves for gamma-ray propagation and absorption through solving for radiative transfer equation with grey opacities.

We set up explosions by initialising balls of material with an exponential density profile with a radial scale height set so that the density at the boundary of the ball is 1 g/cm^3 . Such a setup allows for a mild density contrast near the CSM boundary, which improves the resolution of the shock. For models 1-14, having a type Ia-like engine, we set the ball radius to $0.1R_{\odot}$ and assign it $1.3M_{\odot}$ of C-O material. For model 15, we set a $10M_{\odot}$ ball of $2R_{\odot}$ radius, thus mimicking a core-collapse SN potentially stripped by a companion. The engine acquires the explosion energy split equally into kinetic energy and thermal energy. Furthermore, the kinetic energy is distributed to provide comparable escape velocities for all the velocity bins of ejecta. We have verified that details of the setup, such as the fraction of the explosion energy injected as thermal energy or the initial radius of the explosion ball, have a negligible effect on the lightcurves. We simulate all the models twice, with and without ^{56}Ni . To compare our results to the analytic models of CSM interaction, we use the simulations without ^{56}Ni , and we examine the qualitative effects of ^{56}Ni in the results section 5. For models with ^{56}Ni , we assume $0.6M_{\odot}$ of the radioactive material, typical for type Ia explosions (apart from model 15, wherein we assumed $0.2M_{\odot}$ of ^{56}Ni). The CSM is set up in concentric shells, following the density and composition profiles for the different AGN models, with the full models containing between 1000 and 2000 grid cells. We sample the lightcurves produced in SNEC with a step of 5 minutes to resolve the sharp hour-long peaks in some of the models. Overall, the spherically-symmetric models are initialised similarly to how it is done in the analytic modelling.

The code allows us to trace the detailed properties of the CSM and the shock over time and calculate the lightcurves for the models.

4.3 Effects of the geometry on hydrodynamics and lightcurves

While the SNEC code can deal with most of the relevant physics such as radiative transfer, detailed opacity tables, nuclear energy deposition from ^{56}Ni and ionisation, it cannot model non-spherical geometries. To understand how the supernova ejecta interact with the non-spherical AGN disc material, we carry out additional 2D axisymmetric hydrodynamic simulations of the interaction. For this, we use the hydrodynamic code `HORMONE`, which is a grid-based code that solves the hydrodynamic equations through a Godunov-type scheme (Hirai et al. 2016). We employ an equation of state with contributions from ideal gas and radiation. A spherical coordinate system is used, where we assume axisymmetry with the symmetry axis taken perpendicular to the disc and the coordinate origin placed at the centre of the supernova explosion. In our axisymmetric treatment we ignore any motion of gas in the disc prior to the explosion, such as shearing motion expected in Keplerian discs, and instead treat the disc as an initially static slab of material. We also could not apply the gravity from the central SMBH, so we ignore all gravitational forces, including self-gravity. Therefore, we neglect the initial thermal energy in the disc material too, since it will lead to artificial expansion without the gravitational forces that keep it bound. These assumptions are still valid as long as the time-scale for the shock to reach the surface of the disc is much shorter than the local Keplerian period, and the shock energy is larger than the pre-explosion thermal energy of the disc.

We set up the simulation by placing a slab of material to represent the AGN disc. At the coordinate origin, we place a homogeneously expanding supernova ejecta model with an exponential density profile as

$$\rho_{\text{ej}}(r) = \frac{3\sqrt{6}M_{\text{ej}}}{4\pi v_0^3 t_0^3} \exp\left(-\frac{\sqrt{6}r}{v_0 t_0}\right), \quad (22)$$

where t_0 is the time since explosion. Such exponential profiles are commonly seen in type Ia SN ejecta models (e.g. Nomoto et al. 1984). The velocity profile is set to be $v(r) = r/t_0$. When integrated from 0 to infinity, the total mass is $\int_0^\infty 4\pi r^2 \rho_{\text{ej}} dr = M_{\text{ej}}$ and the total kinetic energy becomes $\int_0^\infty \frac{1}{2} \rho_{\text{ej}}(r) v(r)^2 \cdot 4\pi r^2 dr = E_0$. We cut off the explosion profile at a radius $r = R_{\text{exp}}$ and the time since explosion is set through $t_0 = R_{\text{exp}}/(4v_0)$. The factor 4 is chosen so that the total integrated ejecta mass and energy are still very close to M_{ej} and E_0 . We set a small enough value of R_{exp} such that the mass of the disc material within that radius is negligible compared to the ejecta mass ($\int_0^{R_{\text{exp}}} 4\pi r^2 \rho_{\text{disk}} dr \ll M_{\text{exp}}$), where we can safely assume that the ejecta have freely expanded up to that radius. For all the models presented here, we use an ejecta mass of $M_{\text{ej}} = 1.3 M_\odot$, which represents the ejecta mass for typical type Ia SNe, except for model 15, which has a representative mass of $M_{\text{ej}} = 10M_\odot$, typical for core-collapse SNe.

The ejecta are covered with at least 30 grid points, and the radial grid size is increased as a geometrical series as it goes out. The outer boundary is taken at $\sim 100 H$, and we use ~ 1000 grid points in the radial direction. We divide the polar direction into 400 cells spaced uniformly in $\cos \theta$ so that the solid angle of each cell is equal and the disc is properly resolved.

The lightcurves are estimated through a post-process ray-tracing procedure similar to that of Suzuki et al. (2016). See Appendix D for more details of the lightcurve calculation method.

	L_{44}^{YM19}	L_{44}^{SNEC}	C_L^{YM19}	C_L^{SNEC}
1	1.48	1.7	7.97	9.12
2	0.12	0.14	5.54	<6.48
3	0.26	0.28	4.34	4.69
4	0.62	0.93	5.8	8.6
5	29.38	27.68	10	9.44
6	0.08	0.13	6.63	10.87
7	4.24 ^a	4.42	6.91	7.21
8	24.70 ^b	33.5	1.15	1.56
9	3.96 ^a	7.86	10.65	30.38
10	12.77 ^a	14.90	40.97	26.84
11	7.82 ^a	21.93	10.68	26.82
12	22.55 ^a	5.43	47.2	11.53
13	7.85	2.65	21.05	7.1
14	8.89	14.16	14.69	23.4
15	1.45	1.51	13.45	14.04

Table 2. Peak luminosities and their coefficients. The first column is the model number. The luminosities are normalized to $L_{44} = L/(10^{44} \text{ erg/s})$. The second column is L^{YM19} , the peak luminosity derived from the maximal value of Eq. 20. The third column is the maximum luminosity obtained in SNEC simulation. The fourth column is the ratio $L^{\text{YM19}}/(\rho z^2 v^3)_{\text{bo}}$, which is an estimate for C_L from Eq. 1. The denominator is evaluated at the breakout shell. The last column is the same, only for the numerical maximal SNEC luminosity. a) Evaluated ω at the breakout radius for the analytical fit. b) Used $\omega = 1$.

5 RESULTS

Here we present the analytic and numerical lightcurves for the different models.

5.1 Peak luminosities

In table 2, we show the peak bolometric luminosities from the analytical `YM19` modelling and from SNEC simulations. The last two columns also show the dimensionless prefactor C_L for which the estimate in Eq. 1 matches the relevant luminosity. We see that the peak luminosities from the `YM19` modelling correspond well with the SNEC results for most models. The most discrepant models are 11-13, for which the luminosities differ by factors of 3 to 4.

The estimate of C_L expressed from Eq. 1 shows a discrepancy of up to two orders of magnitude compared to C_L calculated with the previous method. There is no clear trend, and larger values are obtained for models of compact structure and low density, namely the models which explode off-plane (model 9-12) or with a reduced SMBH mass and scale height (model 13) or starved AGN (model 14). Excluding them and the slab model (model 8), which has discontinuous density and is challenging to simulate, leads to a factor of two spread in C_L values, $C_L \approx 7 - 14$ when compared against both `YM19` models and SNEC simulations (models 1,5-7,15). We note that for a spherical model such as the SNEC one, the spherical geometry

suggests the value $C_L = 4\pi \approx 12.6$ for thermalized matter, which is within this range.

We devote the remainder of this section to exploring predicted model lightcurves and their unique features, including comparing numerical and analytical results.

5.2 The lightcurve shape and the effect of changing the energy and ejecta mass

Fig. 3 shows the lightcurves of models 1, 5, 6, which correspond to different explosion energies (10^{51} , 10^{52} and 10^{50} erg, respectively) and also the lightcurve of model 15, which is identical to model 1, but with a larger ejecta mass of $M_{\text{ej}} = 10 M_{\odot}$, which represents a fiducial model of core-collapse SN. We also ran a model with $10 M_{\odot}$ ejecta and a lower energy of 10^{50} erg. The resulting lightcurve peak luminosity is very similar to the low energy of model 6, and is not shown here. Overall we see a good correspondence between the analytical lightcurve (solid) and the numerical results based on the SNEC code (dashed). We see that the larger the energy is, the faster is the breakout time, and the brighter is the peak. The dependence of the peak luminosity on explosion energy is slightly steeper than linear, $L_{\text{peak}} \propto E_0 \Gamma^{(1/2+\mu\omega)\delta^-} \propto E_0^{1+(1/2+\mu\omega)\delta^-}$, which gives the value of 1.28 – 1.29 for our range of density power laws ω_i , where $i = 1, 5, 6$. Γ also depends on l_{eff} , but l_{eff} varies only within 10% between the different models. The additional corrections from l_{eff} slightly change the scaling to 1.23 – 1.24.

Thus, the peak luminosity reaches $\sim 3 \times 10^{45}$ erg s^{-1} for model 5, while it is slightly less than 10^{43} erg s^{-1} for model 6. The different ω 's arise due to the different breakout shells in each model: the less energetic models have a lower velocity by a factor of $E_0^{1/2}$ and hence breakout at later times. The more massive ejecta model 15 has a smaller velocity but has a longer phase of free expansion. Thus its effective power law is $\omega_{15} = 6.04$, which is the largest one in our models. This is due to the fact that in this model, $l_{\text{eff}} = 2.67H$ is very close to the maximal value of $\omega_{15,\text{max}} = 6.076$ obtained at half the photosphere $z_{\text{ph}}/2H = 4.93/2 = 2.465$.

In the spherical phase, the dependence of the luminosity on Γ is a very shallow power law, while the dependence on time since the breakout is $L \propto t^{-x}$ with $x = 0.44 - 0.47$. Note that this is steeper than the maximal slope of -0.35 derived by [Nakar & Sari \(2010\)](#) for radiation dominated material, which is obtained for $\omega = 3$. This is because our extended disc model allows larger values of the effective power law index.

5.3 Changing the SMBH mass and midplane density

Fig. 4 shows the lightcurves of models 4, 13, 14 where the AGN disc structure is altered. In models 4 and 13, the reduced SMBH mass of $10^6 M_{\odot}$, compared to $10^7 M_{\odot}$ for model 13, induces an increase in the midplane density, but the scale height is smaller. Model 4 is exploding at a more distant radial location of $10^4 r_s$, compared to the other two models that explode at $10^3 r_s$, thus making the swept CSM mass larger. While the analytical and SNEC lightcurves broadly agree for model 4, they differ more significantly for models 13 and 14. The general trend is that the SNEC lightcurves decrease more rapidly compared to the analytic ones. The reason may lie in the fact that models 13 and 14 have a reduced CSM interaction mass, which is slightly less than the ejecta mass. Radiative cooling may contribute to the extra drop in the luminosity in the simulations, not accounted for in the analytical model, as discussed in sec. 3.5. Moreover, the peak luminosities in model 13 also differ by a factor of a few. The

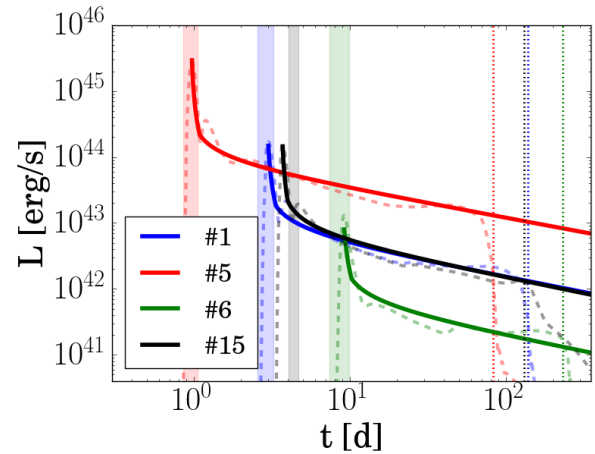


Figure 3. Probing different energies and ejecta masses. The solid lines are the analytical lightcurves where the semi-transparent dashed lines are the SNEC simulations. Model 1 is our canonical model (blue), model 5 has a 10 times higher explosion energy of $E_0 = 10^{52}$ erg (red), model 6 has a 10 times lower explosion energy of $E_0 = 10^{50}$ erg (green). Model 15 (black) has the same explosion energy as model 1, but with larger ejecta mass of $M_{\text{ej}} = 10 M_{\odot}$. The coloured transparent regions indicate the range of possible breakout times as in Fig. 2, with each transparent colour matching the correspondingly coloured model. The vertical dotted lines correspond to the end of the spherical phase for each model shown in their respective colours, also similar to Fig. 2. The effective power laws for the density for each model are $\omega_1 = 5.3$ (the same as in Fig. 2), $\omega_5 = 4.7$, and $\omega_6 = 5.75$, and $\omega_{15} = 6.04$.

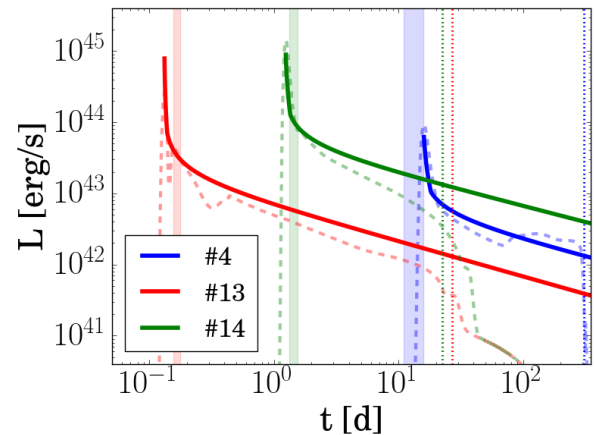


Figure 4. Probing different AGN disc locations and properties. Models 4 and 13 correspond to a $10^6 M_{\odot}$ SMBH, while model 14 corresponds to a $10^7 M_{\odot}$ SMBH. Furthermore, the explosion in model 4 is placed at $10^3 r_s$, while for models 13 and 14, the explosion is placed at $10^4 r_s$. The line style and shaded areas have the same meaning as in Fig. 3. The effective power laws are $\omega_4 = 4.97$, $\omega_{13} = 6.7$, and $\omega_{14} = 4.98$.

difference in the peak luminosities and the wiggles seen in the SNEC lightcurves for model 13 may be related to the reverse shock travelling back through the ejecta. Once the reverse shock reaches the origin of the spherical model, it reflects and starts travelling forward. The reverse shock arrives at the breakout region with a delay compared to the initial forward shock and is typically weaker. The reason the reverse shock is prominent in model 13 is likely because the CSM radius is small compared to other models, and the CSM mass is small enough to allow fast breakout.

5.4 Changing vertical profile

Fig. 5 shows the dependence of the lightcurve on the vertical structure. We see that the radiation-dominated profile (model 7) and the uniform step profile (model 8) lead to progressively earlier and brighter breakouts. This is due to the fact that the respective edges of the different vertical profiles (and also their breakout shells) are more compact than the standard Gaussian profile in model 1.

In Fig. 5, for the calculation of ω we used $l_{\text{edge}} = z_{\text{edge}} - z_{\text{bo}}$ in Eq. 19, where z_{edge} is the physical edge of the disc for model 7, and the photosphere z_{phot} for model 1. The spatial extent of the explosion which enters into the calculation of Γ is unchanged, $l_{\text{eff}} = z_{\text{bo}} - z_1$. The resulting values for these models are $\omega_1^{\text{edge}} = 3.76$ for model 1, and a higher value of $\omega_7^{\text{edge}} = 2.9$ for model 7 (compared to $\omega_7 = 1.46$ in the default choice). For model 7, since z_{bo} is closer to the disc edge, ω_7^{edge} is closer to its limiting value of 3, which is also the power-law suitable for spherical radiative atmospheres. For model 8, the profile is uniform and discontinuous, hence $\omega_8 = 0$ throughout the disc and infinite at the edge. Since ω_8 is ill-defined for model 8, we express the range of possible lightcurves by shading a grey area, where the upper limit is constructed by choosing $\omega_8 = 100$, and the lower limit is given by $\omega_8 = 0$. For comparison, we also plot the analytic fit with $\omega_8 = 1$, which gives a roughly flat lightcurve, similar to the SNEC lightcurve (though we caution that a numerical treatment will also struggle with a discontinuous density profile, and the SNEC models are likely not robust in this case).

For model 1, this fit is comparable to the one with the default choice (as in Figs. 2 and 3). This is also a representative case of all the gas dominated Gaussian profiles, namely that they are not very sensitive to ω . For radiation dominated profiles, however, the latter choice of ω_7^{edge} gives a much better match to the SNEC results. We speculate that the reason may be due to the fact that radiative dominated and slab profiles are more compact and have an actual edge.

5.5 Changing vertical location

Fig. 6 shows the lightcurves of the off-plane explosion models 9–12. Among the Gaussian density profiles, the further out explosion (model 10) at $z_0 = 2H$ explodes earlier and is brighter, as expected. On the other hand, for radiative density profiles, the further explosion (model 12) explodes earlier, but is dimmer than the $z = 1H$ case (model 11). The reason lies in the very low CSM mass for model 12 ($M_{\text{CSM}} < 10^{-3} M_{\odot}$).

The predicted breakout times are compatible with the SNEC models, although for the $z_0 = 2H$ cases, the breakout occurs slightly earlier than expected. The reason may lie again in the low CSM mass, which limits the thermalization of the CSM material. This could account for the large discrepancy between the analytic and numeric lightcurves in model 12.

5.6 Comparison between the codes

Fig. 7 shows the lightcurves of different models and compares predictions from the Lagrangian spherically-symmetric radiative hydrodynamics SNEC code (dashed blue) to those from the Eulerian 2D hydrodynamics HORMONE code (solid black). The goal is to understand how important are the effects of the more realistic 2D disc geometry, including its structure evolution and morphology, since our analytic and SNEC models assume spherical symmetry. The HORMONE simulations do not include radiative transfer and thus radiative cooling

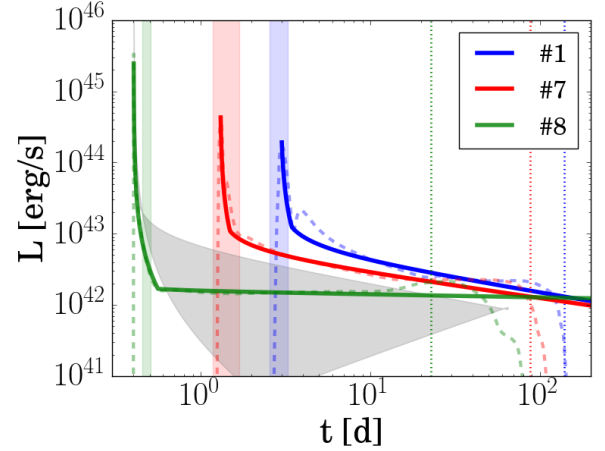


Figure 5. Probing different density profiles. The line style and shaded areas have the same meaning as in Fig. 3. For models 1 and 7, we chose a different location for evaluating ω , at the breakout shell, namely using $l_{\text{edge}} = z_{\text{edge}} - z_{\text{bo}}$, in Eq. 19, where z_{edge} is either the physical edge of the disc (e.g. radiation-dominated profile as in model 7) or the photosphere, if the disc is formally infinite (Gaussian profile as in model 1). The spatial extent l_{eff} which is used to calculate Γ is unchanged. Model 1 is our canonical model (blue), model 8 has a step profile (green), model 7 has a radiation dominated profile (red). The power-law index for model 1 is now $\omega_1^{\text{edge}} = 3.76$, and for model 7 $\omega_7^{\text{edge}} = 2.9$. For model 8, the density profile is infinite at the edge and zero elsewhere. We show the analytic fit for $\omega_8 = 1$ (green). The grey area indicates the possible range of lightcurve for model 8 between the two extremes: $\omega_8 = 0$ is the bottom limit, and $\omega_8 = 100$ as the top limit. The grey area extends up to the peak of the lightcurve.

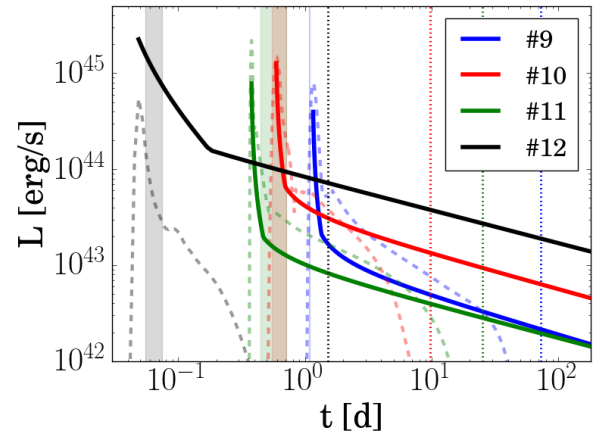


Figure 6. Changing the vertical location of the explosion. Gaussian profiles are for $z_0 = 1H$ (blue, model 9) and $z_0 = 2H$ (red, model 10). Radiative profiles are for $z_0 = 1H$ (green, model 11) and $z_0 = 2H$ (black, model 12). The line style and shaded areas have the same meaning as in Fig. 3. We use the ω^{edge} choice as in fig. 5. The effective power laws are $\omega_9^{\text{edge}} = 3.6$, $\omega_{10}^{\text{edge}} = 3.17$, $\omega_{11}^{\text{edge}} = 2.93$, $\omega_{12}^{\text{edge}} = 2.87$.

and the transfer of energy from the inner parts of the CSM outwards are not properly modelled. However, this only becomes important in the later phases up to and close to shock breakout should be mostly adiabatic. The vertical shock propagation in the 2D HORMONE simulations closely resembles that of the 1D SNEC simulations as shown in Fig. 1.

The lightcurves for the HORMONE models in Fig. 7 are all computed

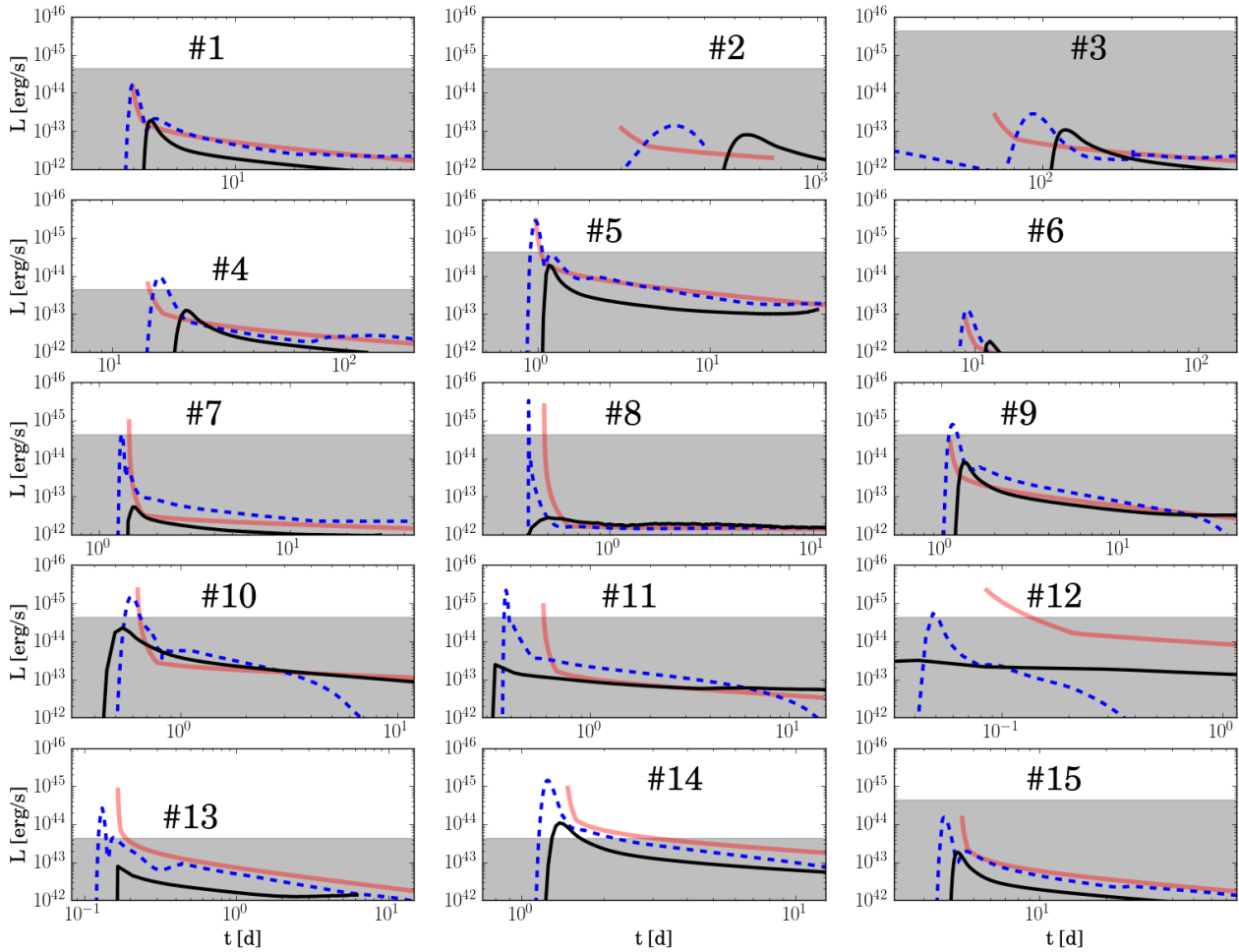


Figure 7. Comparison between the SNEC code (dashed blue) and the HORMONE code (solid black) for all sampled models. The red curve is the analytic fit, but starting with the peak at the average breakout time of the two velocity models calculated in Appendix B, $t_{\text{bo}} = (t_{\text{bo}|_{\text{pw}}} + t_{\text{bo}|_{\text{MM99}}})/2$. The grey area is where the AGN luminosity can obscure the transient. The maximal AGN luminosity is set according to Eq. 23. The model number appears in bold black for each panel. Note that the ordinate is the same, but the abscissa is different for each panel.

for a face-on viewing angle. This is expected to be the angle where the shock breakout is observed with the brightest luminosity. Unlike the spherically symmetric models, the shock breakout in the 2D models starts from a small patch and spreads out radially due to the different shock propagation times along each polar angle. Furthermore, the effective CSM mass the shock has to interact with before breaking out also increases with the polar angle, decreasing the velocity at the breakout shell and making the luminosity at corresponding annuli lower. These differences may likely explain the lower luminosities reached in HORMONE models in Fig. 7. The peak is also smeared out over a slightly longer duration because of the delay in shock breakout at lower latitude angles.

For the off-plane explosions, the difference in interacting mass along each polar angle is smaller compared to the mid-plane explosion models. Therefore, the opening angle of the shock breakout region is wider, leading to more similar peak luminosities between 2D and spherical models (Fig. 7 panels 9, 10).

5.7 Summary of the results

In summary, the typical lightcurve of a SN explosion will peak at luminosities around $10^{44} - 10^{45} \text{ erg s}^{-1}$. The earliest peak will usu-

ally be the brightest one. Radiation-dominated or slab profiles will result in more compact and less massive vertical layers and could produce stronger observable events when compared to gas pressure-dominated (Gaussian) profiles. The type of the SN (or the ejecta mass) will play a relatively minor role in the observational signature, with the main parameter being the explosion energy. This is the case so long as most of the kinetic outflow encounters enough CSM material to reprocess the kinetic energy into outgoing radiation.

The strongest peak will be reached if the CSM mass is comparable to or smaller than the ejecta mass (models 8, 12, 13, 14), although models with CSM mass exceeding the ejecta mass by a factor of ten are also observable. Models with too much CSM mass ($\sim 100M_{\text{ej}}$) will be choked and will not be observable. For these reasons, off-plane explosions, explosions in the inner ($\sim 10^3 r_s$) regions of AGN discs and explosions in the discs of starved AGNs will lead to the brightest transients.

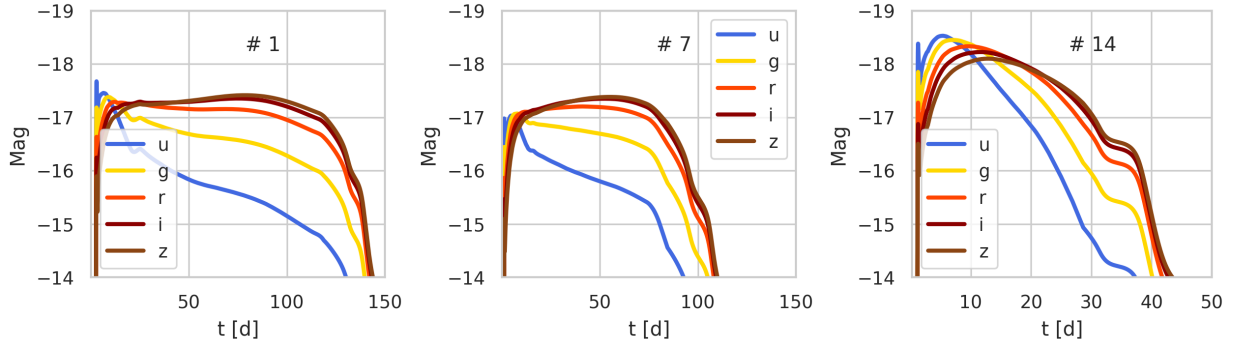


Figure 8. SNEC-based ugriz lightcurves for models 1, 7 and 14. The models represent the CSM interaction signature for a type Ia supernova in a typical AGN around a $10^7 M_{\odot}$ black hole for a pressure-dominated (model 1) and radiation-dominated (model 7) atmospheres, and the same supernova in a starved AGN (model 14). The initial blue/UV half-day-long spike due to shock breakout (which produces the brightest signal in extreme UV / soft X-rays) is followed by the week-long blue/white peak, followed by an extended red/IR emission from the deposited shock energy reprocessed by the CSM. The shape and fall-off times of the lightcurves after the main peak may be inferred from the bolometric lightcurves.

6 DISCUSSION

6.1 Observational picture

Although the SN explosions in AGN disks are typically more luminous than identical explosion in the absence of circumstellar material, they still need to outshine the luminous AGN environment. Hubeny et al. (2001) studied the spectra of AGN accretion discs and found that for a $10^7 M_{\odot}$ disc with a viscosity parameter $\alpha = 0.01$ and luminosity

$$L = 0.3L_{\text{Edd}} = 4.4 \cdot 10^{44} \left(\frac{M_{\bullet}}{10^7 M_{\odot}} \right) \text{erg s}^{-1}, \quad (23)$$

the spectrum peaks at $\nu F_{\nu} \approx 10^{44} \text{ erg s}^{-1}$ in the extreme UV / soft X-ray band around 0.1 keV. In Eq. 23, the Eddington luminosity L_{Edd} assumes the electron scattering opacity.

Bolometric luminosity: For our suite of models, models 1, 6, 9 and 15 peak around $\sim 10^{44} \text{ erg s}^{-1}$ or lower and will likely be obscured by the AGN luminosity in the absence of clear features that make it possible to distinguish AGN spectra from the explosion spectra. Model 4 also peaks around $\sim 10^{44} \text{ erg s}^{-1}$, but the host AGN is less massive. Thus it is a factor of ~ 10 more luminous than the AGN background. Models 5, 8, 10, 11 and 14 peak with luminosities $L \geq 10^{45} \text{ erg s}^{-1}$ and are thus most likely to be observed. Models 13 and 14 are especially promising since they are located in a low-density environment, either in a less massive galaxy or in a starved AGN environment, and could be more luminous than their respective background by a factor of ≥ 100 . We note that this is a conservative estimate, since the observed luminosity can be much lower ($\sim 0.01L_{\text{Edd}}$, Fabian et al. 2009), which will make all models besides 3, 4, and 6 observable.

In summary, the events with the best chances to be observed will be either in a radiation-dominated disc, and/or in a low-density environment. There are three possibilities to achieve this among the set of models we considered: i) in a low mass galaxy ($M \approx 10^9 M_{\odot}$), ii) in a starved AGN of reduced density, or iii) explosions away from the midplane.

Multiband lightcurves: We show the typical multi-band lightcurves in Fig. 8. For all the models, the first breakout will produce a short UV/blue transient, followed by a red/IR tail. As mentioned above, the initial breakout peaks in extreme UV / soft X-rays, so these lightcurves understate the peak bolometric luminosity. The emission is mostly optical after the early breakout peak, which may help to separate these events from the AGN background, which peaks

in UV/X-rays. Furthermore, the models producing sharp peaks, e.g. models 8, 12, 14, reach temperatures high enough to give rise to X-ray flares. In this case, we expect approximately hour-long flares reaching up to 10^{43} erg/s in the 0.3 – 10 keV band. The exceptions to this picture are models 2 and 3, in which the shock stalls due to the large CSM mass. In this case, the thermalised energy is emitted over hundreds of days in red/IR bands.

The presence of ^{56}Ni in real transients will lead to additional energy deposition on a month timescale. However, since the energy is deposited mostly in the ejecta material located behind the CSM, the luminosity contribution from ^{56}Ni will be delayed by the photon diffusion time and eventually emitted over several months or longer in red/IR bands. Since the total energy yield in ^{56}Ni is comparable to that of the regular nuclear transients in the field and since this energy is emitted over longer times, we find that the contribution from radiative decay typically does not exceed 10^{43} erg/s . The AGN will typically outshine such red/IR contributions. Conversely, in models 12-14 with low CSM mass, the CSM lightcurve after the peak becomes quickly dominated by the contribution from the nuclear decay. In this case, the late lightcurve resembles that of isolated supernovae.

The explosion and its ejecta are expected to be non-relativistic. It is possible that some fraction of the electrons, especially where the temperature is large enough, will not be in thermal equilibrium and will be accelerated to relativistic velocities producing γ -rays, either in GRBs (Zhu et al. 2020; Perna et al. 2021b) or in hyper-Eddington accretion-induced Bondi explosions (Wang et al. 2021), where due to inefficient energy transport the material is heated to very large temperatures, and relativistic shocks make a large cavity in the AGN disc. While the GRB radiation is a prompt emission, the radiation from Bondi explosions will be visible only in the broad-line region, $\sim 1 \text{ yr}$ after the explosion. For GRBs, following the cocoon breakout, non relativistic ejecta also break out at later times. We find similar peak luminosities to the estimates of Zhu et al. (2020).

6.2 Rates of SNe in AGN discs

The radiative efficiency of an accreting AGN is $\eta = L/(\dot{M}c^2) < 1$. If the SMBH is accreting at a fraction $L = fL_{\text{Edd}}$ of the Eddington luminosity, and the same fraction f of the mass accretion rate, the SMBH mass doubling time is

$$t_{\text{doubling}} = \frac{M_{\bullet}}{\dot{M}} = \frac{\eta}{f} \frac{\kappa c}{4\pi G} = 128 \left(\frac{\eta}{0.1} \right) \left(\frac{f}{0.3} \right)^{-1} \text{Myr}. \quad (24)$$

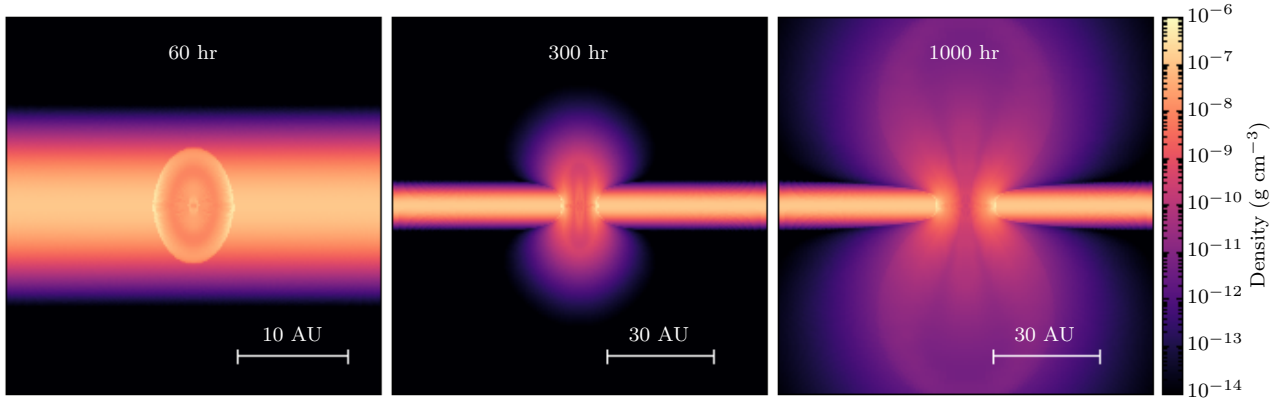


Figure 9. Density snapshots from the 2D simulations for model 1. Each panel shows a different time snapshot. Note that the left panel has a smaller box size.

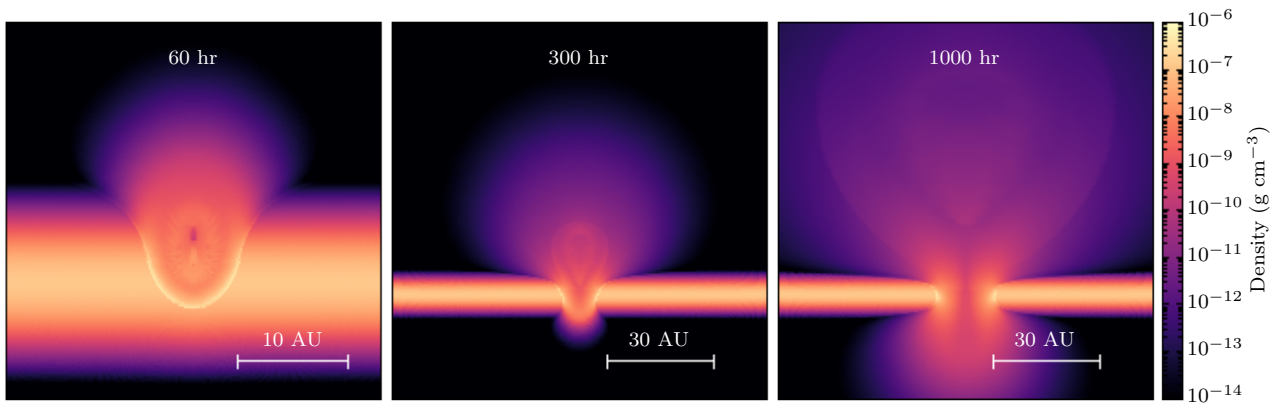


Figure 10. Same as Fig. 9 but for model 9.

For a disc lifetime of $t_{\text{AGN}} = 10^8$ yr, the mass that flows into the disc is $M_{\bullet} t_{\text{AGN}} / t_{\text{doubling}} \approx M_{\bullet}$.

The type Ia SN rate is 1 per few hundred solar masses of star formation in the field (Maoz & Graur 2017). Assuming a similar but slightly higher efficiency for AGN discs due to an enhanced binary merger rate (e.g., one SN event per $100M_{\odot}$), and further assuming a fraction f_1 is converted into stars, we would have $f_1 10^5$ SNe for a SMBH mass of $10^7 M_{\odot}$ over an AGN lifetime $t_{\text{AGN}} = 10^8$ yr. Thus, the rate per AGN is $f_1 10^{-3} \text{ yr}^{-1}$ per AGN disc. Roughly 1% galaxies in the local Universe have an AGN disc, so the AGN density is 10^{-4} Mpc^{-3} . Thus, we expect a total of $\sim f_1 100$ AGN SNe per Gpc^3 per year. A similar estimate for the rate of core-collapse SNe leads to a slightly higher but otherwise comparable rate of events. This rate is also slightly larger than the the upper limit of the binary black hole merger rate in AGN discs, $\mathcal{R} = 0.002 - 18 \text{ Gpc}^{-3} \text{ yr}^{-1}$, which had been recently estimated by Gröbner et al. (2020).

A proper rate estimate should include an integral over the mass function of the AGN in the local universe. Moreover, indirect observations of the AGN phase duration ($10^6 - 10^9$ yr), and hence the duty cycle ($10^{-1} - 10^{-3}$), could vary by around one order of magnitude (Martini & Weinberg 2001; Marconi et al. 2004). Furthermore, AGNs may not be accreting steadily but rather experience events of

rapid accretion and quiescence every 10^5 years (Schawinski et al. 2015) which could affect the star formation rate.

6.3 Observable event rates

What fraction of the SNe will be observable? In order to address this question, we need to discuss the spatial distribution of stars in AGN discs, the mass function of the formed stars and its dependence on accretion.

Star formation in AGN discs predominantly occurs in the outer regions of the disc at low temperatures, where the disc is gravitationally unstable. The star formation efficiency is especially large when the midplane temperature is between $10^3 - 10^4$ K, and the opacity is very low since dust is still vaporized, but the material is mostly neutral, so electron scattering is low.

Migration: The interaction of the stars with the massive gaseous AGN discs can induce torques on them and cause the stars to migrate (e.g. Artymowicz et al. 1993; McKernan et al. 2012; Bellovary et al. 2016, and references therein). Migration can be stopped if the torque changes sign. Extensive work had been done on migration in protoplanetary discs (Goldreich & Tremaine 1980; Tanaka et al. 2002; Paardekooper & Mellema 2006; Paardekooper et al. 2010), and migration traps were numerically reproduced (Lyra et al. 2010).

Bellovary et al. (2016) found that the outermost migration traps for AGN discs lie at around $\sim 300r_g$. If most stars end up in this region, the binary mergers and SN explosions there will be both more frequent and more observable.

However, AGN discs are not necessarily as well behaved as protoplanetary discs. The immense radiation and mass make them prone to flaring and instabilities. It is uncertain whether the disc structure of SG03 and Thompson et al. (2005) is in a steady state, and the fitting formulae for the torque as in Paardekooper et al. (2010) may not be applicable. Moreover, Bellovary et al. (2016) used an adiabatic index of $\gamma = 5/3$. Radiation-dominated discs with $\gamma = 4/3$ will result in a different location for the migration traps, which may be shifted outwards.

Another issue is the timescale for the migration to take place. For type I migration, in which viscous torques are unable to form a gap in the disc, the migration time is (Tanaka et al. 2002)

$$\tau_I \sim \frac{M_\bullet^2}{M_\odot \Sigma(r) r^2} \left(\frac{H}{r}\right)^2 \Omega^{-1} = 7 \left(\frac{M_\bullet}{10^7 M_\odot}\right)^2 \left(\frac{r}{10^4 r_s}\right)^2 \text{ Myr} \quad (25)$$

Stars that formed beyond $10^5 r_s$ or in more massive discs would require longer than the lifetime of the disc to migrate, while less massive discs enable faster, more efficient migration. In some very low mass discs, a gap may be carved, and the migration timescale will be of type II, which will not depend on the mass of the disc (or the SMBH mass). Stars may still be captured from the nuclear star cluster onto the AGN disc.

Finally, the dynamical friction experienced by the stars could be significantly different from these simple estimates if the accretion onto the stars produces strong outflows (Gruzinov et al. 2020), which is almost inevitable for the AGN environment where the accretion rates can be well above the Eddington limit (also see below).

The spatial distribution of the progenitors of SN explosions will depend on the migration history. Since the shocks from explosions at radial distances beyond $r \gtrsim 10^3 r_s$ will be choked, the number of observed progenitors in the disc will be $N_3 = N(r \lesssim 10^3 r_s)$. If migration is effective, most of the progenitors may be close to the migration traps, yielding a fraction of observed events $f_2 = N_3/N_{\text{tot}} \sim 1$, where N_{tot} is the total number of the progenitors. If no migration occurs, then assuming an underlying log-uniform distribution between $10^2 - 10^5 r_s$, only $f_2 \sim 0.3$ of the events will be observable. If most stars are either stuck in the outer regions or migrate outward, then $f_2 \ll 1$ could be rather low.

Accretion: Accretion could be important for changing the initial mass function of stars in AGN discs and affecting the type Ia / core-collapse SN branching ratios. However, neither the details of the expected super-Eddington accretion nor the initial mass function are certain. Artymowicz et al. (1993) first studied the growth and accretion of stars in AGN discs. More recently, Davies & Lin (2020); Cantiello et al. (2020) suggested that significant growth can occur. Leigh et al. (2013) also had a similar discussion, with possible implications for depleting the gas through accretion. However, a recent follow-up study showed that rotation and radiative feedback could limit the final mass to be around $10 M_\odot$ (Jermyn et al. 2021), especially for the innermost regions, which we mainly consider. Moreover, the extremely optically thick environment may block the energy release via radiation and inhibit the accretion rate. A similar situation could lead to "Bondi explosions" (Wang et al. 2021).

Accretion onto white dwarfs might, under appropriate conditions, allow for their growth to close to the Chandrasekhar limit and eventual explosion as type Ia SNe Ostriker (1983), thus increasing the rate for such events. However, here too, the exact accretion efficiency is difficult to assess.

The frequency of off-plane explosions is also quite uncertain, but probably low. Gas dynamical friction tends to damp the orbital inclination much faster than the migration timescale (Rein 2012; Grishin & Perets 2015) if the orbital inclination with respect to the disc midplane is not too large. Highly inclined orbits ($i \gg H/r$) may take much longer to dissipate into the plane of the disc, but they spend most of their time outside of the disc, and are therefore likely to explode in relative isolation without significant CSM interaction. Accretion feedback may change this picture (Gruzinov et al. 2020), while close encounters with neighbouring stars may excite the progenitors' orbits.

To summarize, the upper limit for the rates of detectable events is $\mathcal{R} \lesssim f_1 f_2 100 \text{ yr Gpc}^{-3}$, where f_1 is the efficiency of forming AGN gas into stars, and f_2 is the fraction of observable events. The fraction of core-collapse SNe is uncertain and could constrain the efficiency of accretion or the underlying mass function.

Remaining agnostic to the efficiency of accretion and its final fate, we comment that for a Salpeter mass function $dN/dm \propto m^{-2.35}$, around 1% of stars are born massive enough to produce core-collapse SN explosions, while for a top-heavy mass function $dN/dm \propto m^{-0.45}$ (Bartko et al. 2010), the fraction of massive stars increases to $\sim 10\%$, thus increasing the rates by an additional factor of ten.

6.4 Disc feedback

The 2D hydrodynamical simulations allow us to explore the morphology of the ejecta and the impact on the local disc morphology around the explosion site. Fig. 9 shows density snapshots of model 1. We see that at the early time of 60 hr, shortly before shock breakout (left panel), the blast wave is still rather spherical, expanding within the disc. The shock front is gradually deformed as the in-plane directions are pinched, and the shock front propagates faster in the vertical directions, making the blast wave take a prolate form. Later, the shock breaks out from the disc surface, and a local hole is carved in the disc. The ejecta flow out almost spherically from the location of shock breakout.

The overall features are qualitatively similar to recent 3D numerical simulations of an SN explosion in a more distant radial location ($M_\bullet = 10^8 M_\odot, r = 2 \cdot 10^4 r_s$; Moranchel-Basurto et al. 2021). Due to the larger spatial extent and higher interaction mass, the more distant event will not be observable. However, SN explosions may contribute to the global viscous evolution of the AGN disc. The 2D simulations we present do not take into account the shearing motions of the disc. In reality, the hole excavated by the SN will be elongated in the disc rotation direction (Moranchel-Basurto et al. 2021).

Fig. 10 shows the density snapshots of the off-plane explosion, model 9. We see that the shock breaks out earlier from the top edge, while the downward shock propagates longer as it climbs up the density gradient. This downwards CSM interaction creates a strong upwards reverse shock, which quickly flows out through the upper hole. The downwards shock also eventually breaks out from the other side of the disc. The breakout from this side of the disc is much weaker than the upper side, and the luminosity should be much dimmer.

6.5 AGN flaring and variability

The significant variability observed for AGNs over a wide range of timescales gives rise to difficulties in identifying nuclear transients and separating such transients from various forms of inherent AGN variability.

As discussed above, the observational signatures of SNe in AGN

discs resulting from our models suggest that the SN transients will often be challenging to observe above the background luminosity of the AGN. However, in some cases, these AGN SNe can surpass the AGN background during their rapid rise to a peak. The timescale for such initial high-luminosity flaring is of the order of hours up to 1-2 days at most (see sec. 5). Identifying such short-term transients requires high-cadence transient surveys. Moreover, many transient surveys do not focus on AGN nuclear regions where the AGN variability challenges identification. To the best of our knowledge, the only high-cadence sky surveys of AGNs were done using the Kepler mission. Interestingly, these surveys did identify one fast, days-timescale flare event KIC 1606852 (Smith et al. 2018), which could potentially be related to the AGN SNe we discuss. However, it might be too long or be the result of other explosive processes (Smith et al. 2018). The timescale of other nuclear transients, such as candidate tidal disruption events and changing-look AGNs, are far longer than the peak timescale of AGN SNe and are not likely to be related. Future high-cadence transient surveys may be able to identify AGN SNe.

7 SUMMARY

The AGN disc environment around SMBHs has dense stellar populations, many of which are expected to be embedded in the disc. As stars end their lives in supernova explosions, the dense AGN environment makes a fertile ground for unique transient events. Understanding such explosions and their properties opens a window to the physics of AGN discs and their interactions with the supernova progenitors.

Motivated by superluminous explosions in circumstellar material (CSM), we have developed an analytical model for the expected time of breakout and subsequent lightcurve, depending on the disc and progenitor properties. We validated this model with extensive numerical simulations. We found that the typical peak luminosity for such events may reach a few times 10^{45} erg s^{-1} . The most energetic events are also the quickest to break out, ranging from hours to several days, until they become too faint to be detected.

The most luminous explosions are generally found either in radiation-dominated discs, at larger explosion energies, or in regions with reduced density, such as off-plane explosions, low mass SMBH, or starved AGNs with reduced density. The latter two (i.e. low SMBH mass and starved AGN discs) also have better chances of being observed due to reduced background AGN luminosity. The initial breakout events should be dominated by the blue bands, while at later times, the lightcurves will be dominated by the red and infrared bands. The upper limit for the event rate is $\mathcal{R} \lesssim 100$ yr Gpc^{-3} , where optimal star formation and observational conditions are assumed. The actual rate could be lower by orders of magnitude.

In concise form, our study may be summarised as follows: *We exploded stars in an AGN. The photons can't get out, the outflow can. The gas converts shocks into brighter SN. We may see a few hundred, if we frequently scan.*

DATA AVAILABILITY

The simulations underlying this article will be shared on reasonable request to the corresponding author.

ACKNOWLEDGEMENTS

We thank the referee, Pablo Fabián Velázquez, for valuable comments on the manuscript. We thank Almog Yalinewich, Ari Laor and Yossef Zenati for stimulating discussions. EG and HBP acknowledge support for this project from the European Union's Horizon 2020 research and innovation program under grant agreement No 865932-ERC-SNeX. IM is a recipient of the Australian Research Council Future Fellowship FT190100574.

REFERENCES

- Artymowicz P., Lin D. N. C., Wampller E. J., 1993, *ApJ*, 409, 592
 Bartko H., et al., 2010, *ApJ*, 708, 834
 Baruteau C., Cuadra J., Lin D. N. C., 2011, *ApJ*, 726, 28
 Bellovary J. M., Mac Low M.-M., McKernan B., Ford K. E. S., 2016, *ApJ*, 819, L17
 Cantiello M., Jermyn A. S., Lin D. N. C., 2020, arXiv e-prints, p. arXiv:2009.03936
 Cheng K. S., Wang J.-M., 1999, *ApJ*, 521, 502
 Chevalier R. A., Irwin C. M., 2011, *ApJ*, 729, L6
 Davies M. B., Lin D. N. C., 2020, *MNRAS*, 498, 3452
 Davis S. W., Tchekhovskoy A., 2020, *ARA&A*, 58, 407
 Dessart L., Audit E., Hillier D. J., 2015, *MNRAS*, 449, 4304
 Dittmann A. J., Miller M. C., 2020, *MNRAS*, 493, 3732
 Fabian A. C., Vasudevan R. V., Mushotzky R. F., Winter L. M., Reynolds C. S., 2009, *MNRAS*, 394, L89
 Ferguson J. W., Alexander D. R., Allard F., Barman T., Bodnarik J. G., Hauschildt P. H., Heffner-Wong A., Tamanai A., 2005, *ApJ*, 623, 585
 Ferrara A., Tolstoy E., 2000, *MNRAS*, 313, 291
 Gal-Yam A., 2019, *ARA&A*, 57, 305
 Ginzburg S., Balberg S., 2012, *ApJ*, 757, 178
 Goldreich P., Tremaine S., 1980, *ApJ*, 241, 425
 Goldreich P., Lithwick Y., Sari R., 2002, *Nature*, 420, 643
 Grishin E., Perets H. B., 2015, *ApJ*, 811, 54
 Gröbner M., Ishibashi W., Tiwari S., Haney M., Jetzer P., 2020, *A&A*, 638, A119
 Gruzinov A., Levin Y., Matzner C. D., 2020, *MNRAS*, 492, 2755
 Hirai R., Nagakura H., Okawa H., Fujisawa K., 2016, *Phys. Rev. D*, 93, 083006
 Hirose S., Krolik J. H., Blaes O., 2009, *ApJ*, 691, 16
 Hubeny I., Blaes O., Krolik J. H., Agol E., 2001, *ApJ*, 559, 680
 Iglesias C. A., Rogers F. J., 1996, *ApJ*, 464, 943
 Janka H.-T., 2012, *Annual Review of Nuclear and Particle Science*, 62, 407
 Jermyn A. S., Dittmann A. J., Cantiello M., Perna R., 2021, arXiv e-prints, p. arXiv:2102.13114
 Jiang Y.-F., Stone J. M., Davis S. W., 2013, *ApJ*, 778, 65
 Jiang Y.-F., Davis S. W., Stone J. M., 2016, *ApJ*, 827, 10
 Leigh N. W. C., Böker T., Maccarone T. J., Perets H. B., 2013, *MNRAS*, 429, 2997
 Lynden-Bell D., 1969, *Nature*, 223, 690
 Lyra W., Paardekooper S.-J., Mac Low M.-M., 2010, *ApJ*, 715, L68
 Maoz D., Graur O., 2017, *ApJ*, 848, 25
 Marconi A., Risaliti G., Gilli R., Hunt L. K., Maiolino R., Salvati M., 2004, *MNRAS*, 351, 169
 Martini P., Weinberg D. H., 2001, *ApJ*, 547, 12
 Matzner C. D., McKee C. F., 1999, *ApJ*, 510, 379
 McKernan B., Ford K. E. S., Lyra W., Perets H. B., 2012, *MNRAS*, 425, 460
 McKernan B., Ford K. E. S., O'Shaughnessy R., 2020, *MNRAS*, 498, 4088
 Miralda-Escudé J., Gould A., 2000, *ApJ*, 545, 847
 Moranchel-Basurto A., Sánchez-Salcedo F. J., Chametla R. O., Velázquez P. F., 2021, *ApJ*, 906, 15
 Moriya T. J., Maeda K., Taddia F., Sollerman J., Blinnikov S. I., Sorokina E. I., 2013, *MNRAS*, 435, 1520
 Morozova V., Ott C. D., Piro A. L., 2015a, SNEC: SuperNova Explosion Code (ascl:1505.033)

Morozova V., Piro A. L., Renzo M., Ott C. D., Clausen D., Couch S. M., Ellis J., Roberts L. F., 2015b, *ApJ*, **814**, 63
 Morozova V., Piro A. L., Valenti S., 2017, *ApJ*, **838**, 28
 Nakar E., Piro A. L., 2014, *ApJ*, **788**, 193
 Nakar E., Sari R., 2010, *ApJ*, **725**, 904
 Nomoto K., Thielemann F. K., Yokoi K., 1984, *ApJ*, **286**, 644
 Ostriker J. P., 1983, *ApJ*, **273**, 99
 Paardekooper S. J., Mellema G., 2006, *A&A*, **459**, L17
 Paardekooper S. J., Baruteau C., Crida A., Kley W., 2010, *MNRAS*, **401**, 1950
 Paczynski B., 1978, *Acta Astron.*, **28**, 91
 Perets H. B., Li Z., Lombardi James C. J., Milcarek Stephen R. J., 2016, *ApJ*, **823**, 113
 Perna R., Tagawa H., Haiman Z., Bartos I., 2021a, arXiv e-prints, p. arXiv:2103.10963
 Perna R., Lazzati D., Cantiello M., 2021b, *ApJ*, **906**, L7
 Piro A. L., Haynie A., Yao Y., 2020, arXiv e-prints, p. arXiv:2007.08543
 Rein H., 2012, *MNRAS*, **422**, 3611
 Rozyczka M., Bodenheimer P., Lin D. N. C., 1995, *MNRAS*, **276**, 597
 Sakurai A., 1960, *Communications on Pure and Applied Mathematics*, **13**, 353
 Schawinski K., Koss M., Berney S., Sartori L. F., 2015, *MNRAS*, **451**, 2517
 Sedov L. I., 1946, *Prikl. Mat. Mekh.*, **10**, 241
 Semenov D., Henning T., Helling C., Ilgner M., Sedlmayr E., 2003, *A&A*, **410**, 611
 Shakura N. I., Sunyaev R. A., 1973, *A&A*, **500**, 33
 Shakura N., Sunyaev R., 1976, *Monthly Notices of the Royal Astronomical Society*, **175**, 613
 Sirko E., Goodman J., 2003, *MNRAS*, **341**, 501
 Smith K. L., Mushotzky R. F., Boyd P. T., Malkan M., Howell S. B., Gelino D. M., 2018, *ApJ*, **857**, 141
 Suzuki A., Maeda K., Shigeyama T., 2016, *ApJ*, **825**, 92
 Suzuki A., Moriya T. J., Takiwaki T., 2019, *ApJ*, **887**, 249
 Suzuki A., Nicholl M., Moriya T. J., Takiwaki T., 2021, *ApJ*, **908**, 99
 Syer D., Clarke C. J., Rees M. J., 1991, *MNRAS*, **250**, 505
 Tagawa H., Haiman Z., Kocsis B., 2020, *ApJ*, **898**, 25
 Takei Y., Shigeyama T., 2020, *PASJ*, **72**, 67
 Tanaka H., Takeuchi T., Ward W. R., 2002, *ApJ*, **565**, 1257
 Taylor G., 1950, *Proceedings of the Royal Society of London Series A*, **201**, 159
 Thompson T. A., Quataert E., Murray N., 2005, *ApJ*, **630**, 167
 Tsuna D., Kashiyama K., Shigeyama T., 2019, *ApJ*, **884**, 87
 Utrobin V. P., 2007, in Immler S., Weiler K., McCray R., eds, *American Institute of Physics Conference Series Vol. 937, Supernova 1987A: 20 Years After: Supernovae and Gamma-Ray Bursters*. pp 25–32, doi:10.1063/1.3682879
 Wang J.-M., Liu J.-R., Ho L. C., Du P., 2021, arXiv e-prints, p. arXiv:2103.07708
 Woosley S. E., Blinnikov S., Heger A., 2007, *Nature*, **450**, 390
 Yalinewich A., Matzner C. D., 2019, *MNRAS*, **490**, 312
 Zhu J.-P., Zhang B., Yu Y.-W., Gao H., 2020, arXiv e-prints, p. arXiv:2011.08428
 Zhu J.-P., Wang K., Zhang B., Yang Y.-P., Yu Y.-W., Gao H., 2021a, arXiv e-prints, p. arXiv:2103.00789
 Zhu J.-P., Yang Y.-P., Zhang B., Liu L.-D., Yu Y.-W., Gao H., 2021b, arXiv e-prints, p. arXiv:2104.09389

APPENDIX A: VERTICAL PROFILE FOR RADIATION-DOMINATED PRESSURE

Consider the radiation pressure $P = aT^4/3 = K\rho^{4/3}$, where $a = 4\sigma_{\text{SB}}/c$, σ_{SB} is the Stefan-Boltzmann constant and c is the speed of light. We assume a polytropic equation of state where $P = K\rho^\gamma$. The sound speed is given by $c_s = \sqrt{dP/d\rho} = \sqrt{\gamma K\rho^{\gamma-1}} = \sqrt{\gamma P/\rho}$. The

vertical hydrostatic equilibrium equation is

$$\frac{dP}{dh} = -\rho g_z = K\gamma\rho^{\gamma-1} \frac{d\rho}{dh} \quad (\text{A1})$$

where $g_z = GM_{\text{SMBH}}h/(r^2 + h^2)^{3/2}$ is the z component of the tidal gravitational acceleration. Since the disc is thin ($h \ll R$), we can approximate it as $g_z \approx \Omega^2 h$ where $\Omega^2 = GM_{\text{SMBH}}/r^3$ is the Keplerian frequency. We have the ordinary differential equation

$$\rho^{\gamma-2} d\rho = -\frac{\Omega^2}{\gamma K}. \quad (\text{A2})$$

Integrating, we have

$$\frac{\rho^{\gamma-1}}{\gamma-1} = -\frac{\Omega^2}{2\gamma K} z^2 + C. \quad (\text{A3})$$

To determine C we use the initial condition at $h = 0$

$$\rho^{\gamma-1} = (\gamma-1)C = \rho_0^{\gamma-1} \implies C = \rho_0^{\gamma-1}/(\gamma-1). \quad (\text{A4})$$

Finally, the vertical profile is

$$\rho(h) = \rho_0 \left[1 - (\gamma-1) \frac{\Omega^2}{2\gamma K \rho_0^{\gamma-1}} h^2 \right]^{1/(\gamma-1)}. \quad (\text{A5})$$

Note that the scale height H is defined as

$$H^{-2} = \frac{\Omega^2}{c_s^2} = \frac{\Omega^2}{\gamma K \rho_0^{\gamma-1}}, \quad (\text{A6})$$

which leads to the final expression

$$\rho_{\text{rad}}(h) = \rho_0 \left[1 - (\gamma-1) \frac{h^2}{2H^2} \right]^{1/(\gamma-1)}. \quad (\text{A7})$$

Note that the radiation pressure-dominated profile is steeper than the Gaussian profile $\rho_{\text{gas}} \propto \exp(-h^2/2H^2)$ for gas dominated pressure $P \propto \rho$, and goes to zero at $h/H = \sqrt{2/(\gamma-1)}$, or $h/H = \sqrt{6} \approx 2.45$.

APPENDIX B: BREAKOUT TIMES IN AGN DISCS

Gaussian density profile: For the piecewise velocity (Eq. 12) in the Gaussian density profile (Eq. 4) the integral in Eq. 14 can be split into three integrals. The first one over the free expansion phase is trivial, while the other two involve integrals of the form $\int x^{3/2} e^{-\alpha x^2/2} dx = -2^{1/4} \Gamma(5/4, \alpha x^2/2) / \alpha^{5/4}$, where $\Gamma(s, x) = \int_x^\infty y^{s-1} e^{-y} dy$ is the upper incomplete Gamma function. We get

$$\begin{aligned} \frac{t_{\text{bo}}}{H/v_{\text{pw}}} \Big|_{\text{pw}} = & \zeta_1 + \frac{2^{1/4} \mathcal{A}_1}{\zeta_1^{3/2} \mu^{5/4}} \left[\Gamma\left(\frac{5}{4}, \frac{\mu' \zeta_1^2}{2}\right) - \Gamma\left(\frac{5}{4}, \frac{\mu' \zeta_2^2}{2}\right) \right] \\ & + \frac{2^{1/4} \mathcal{A}_2}{\zeta_1^{3/2} \mu^{5/4}} \left[\Gamma\left(\frac{5}{4}, \frac{\mu \zeta_2^2}{2}\right) - \Gamma\left(\frac{5}{4}, \frac{\mu \zeta_{\text{bo}}^2}{2}\right) \right] \end{aligned} \quad (\text{B1})$$

where $\zeta_i, \zeta_{\text{bo}} = z_i/H, z_{\text{bo}}/H$ are dimensionless length scales, $\mathcal{A}_1 = (\rho_0/\rho_1)\mu'$ and $\mathcal{A}_2 = (\rho_2/\rho_1)\mu'(\rho_0/\rho_1)^\mu$ are coefficients that depend on the density at each location, which comes from the continuity requirements of the piecewise velocity in Eq. (12). For the parameters of model 1, we get $t_{\text{bo}} = 3.17$ d.

For the MM99 velocity model (Eq. 13) in the Gaussian profile, the breakout time is given by

$$t_{\text{bo}}|_{\text{MM99}} = \frac{H}{v_0} \int_0^{\zeta_{\text{bo}}} \left(1 + \frac{\rho_0 H^3}{M_{\text{ej}}} \zeta^3 \right)^{1/2} e^{-\mu \zeta^2/2} d\zeta. \quad (\text{B2})$$

This is not an analytic expression, but can be evaluated numerically. For model 1, the breakout time is around 2.55 d, which is shorter by a factor of $\sim 17\%$. Generally, as seen in Fig. 1, the shock velocity obtained by simulations is somewhere in between the piecewise model and the MM99 model. We compare to the numerical results in sec. 4.

Radiation-dominated density profile: For the piecewise velocity in the radiation-dominated profile (Eq. 5), the integrals are similar. They have the form

$$J(y, \alpha) = \int y^{3/2} \left(1 - \frac{y^2}{6}\right)^{3\alpha} dy = \frac{2}{5} y^{2/5} {}_2F_1\left(\frac{5}{4}, -3\alpha, \frac{9}{4}, \frac{y^2}{6}\right), \quad (\text{B3})$$

where ${}_2F_1(a, b, c, x)$ is the hypergeometric function. The breakout time is

$$\frac{t_{\text{bo}}}{H/v_0}\Big|_{\text{pw}} = \zeta_1 + \frac{\mathcal{A}_1}{\zeta_1^{3/2}} [J(\zeta_2, 3\mu') - J(\zeta_1, 3\mu')] + \frac{\mathcal{A}_2}{\zeta_1^{3/2}} [J(\zeta_{\text{bo}}, 3\mu) - J(\zeta_2, 3\mu)]. \quad (\text{B4})$$

For the MM99 velocity model in the radiation-dominated profile, the breakout time is given by

$$t_{\text{bo}}|_{\text{MM99}} = \frac{H}{v_0} \int_0^{\zeta_{\text{bo}}} \left(1 + \frac{\rho_0 H^3}{M_{\text{ej}}} \zeta^3\right)^{1/2} \left(1 - \frac{\zeta^2}{6}\right)^{3\mu} d\zeta, \quad (\text{B5})$$

which is, again, not analytic but can be estimated numerically.

Off-plane explosions: For off-plane explosions the integrals are the same but the integration domain is $(\zeta_0, \zeta_{\text{bo}})$, where ζ_0 is the explosion site above the midplane. For the MM99 model this is the only change.

For the piecewise model, we divide the domain into three regions, corresponding to the piecewise velocity solution in Eq. 12, namely

$$t_{\text{bo}} = \frac{H}{v_0} (I_1 + I_2 + I_3). \quad (\text{B6})$$

Here, $I_1 = \zeta_1 - \zeta_0$, is the integral over the (constant velocity v_0) free expansion phase; I_2 is the integral between ζ_1 and ζ_2 , where the velocity scales with the density with a power law $v \propto \rho^{-\mu'}$, where $\mu' = \mu + 1/5$; and I_3 is the integral between ζ_2 and ζ_{bo} , where the velocity scales with the density with a power law $v \propto \rho^{-\mu}$.

For $\zeta_{\text{bo}} > \zeta_2 > \zeta_1 > \zeta_0$, the result is essentially the same as in Eq. B1, but with I_1 replacing ζ_1 in the first term. This is the case for model 9.

For $\zeta_1 < \zeta_{\text{bo}} < \zeta_2$, the shock breaks out before the Sakurai acceleration begins. This leads to $I_3 = 0$ and the domain of integration of I_2 is $(\zeta_1, \zeta_{\text{bo}})$. This is the case for models 10 and 11.

For $\zeta_{\text{bo}} < \zeta_1$, the shock breaks out before the free expansion phase ends. In this case, we only have $I_1 = \zeta_{\text{bo}} - \zeta_1$. This is the case for model 12.

APPENDIX C: CSM MASS

Here we explicitly calculate the integral in Eq. (21) for various models. We will start with mid-plane explosions and hence fix $z_{\text{min}} = 0$.

For a flat profile, $z_{\text{max}} = H$ and the CSM mass is simply $M_{\text{CSM}} = 4\pi\rho_0 H^3/3$.

For the Gaussian profile we have

$$\begin{aligned} M_{\text{CSM}}(z_{\text{max}}) &= 4\pi\rho_0 \int_0^{z_{\text{max}}} e^{-z^2/2H^2} z^2 dz \\ &= 4\pi\rho_0 H^3 \left[\sqrt{\frac{\pi}{2}} \operatorname{erf}\left(\frac{z_{\text{max}}}{\sqrt{2}}\right) - \frac{z_{\text{max}}}{\sqrt{2}} e^{-z_{\text{max}}^2/2} \right] \end{aligned} \quad (\text{C1})$$

where $\zeta_{\text{max}} = z_{\text{max}}/H$. Note that for $\zeta_{\text{max}} \rightarrow \infty$ we get $M_{\text{CSM},\infty} = (2\pi)^{3/2} \rho_0 H^3$ while for small $\zeta_{\text{max}} \ll 1$ it is essentially as the uniform density case, $M_{\text{CSM}}(z_{\text{max}} \ll H) \approx 4\pi\rho_0 z_{\text{max}}^3/3$. For all practical purposes, the value at the photosphere is close enough to the limiting value.

For the radiation-dominated profile, we have

$$\begin{aligned} M_{\text{CSM}}(z_{\text{max}}) &= 4\pi\rho_0 \int_0^{z_{\text{max}}} \left(1 - \frac{z^2}{6H^2}\right)^3 z^2 dz \\ &= 4\pi\rho_0 H^3 \left[\frac{\zeta_{\text{max}}^3}{3} - \frac{\zeta_{\text{max}}^5}{10} + \frac{\zeta_{\text{max}}^7}{84} - \frac{\zeta_{\text{max}}^9}{1944} \right] \end{aligned} \quad (\text{C2})$$

For the maximal value $\zeta_{\text{max}} = \sqrt{6}$ we have $M(z_{\text{max}}) = 4\pi\rho_0 H^3 \times \frac{32}{35} \sqrt{\frac{2}{3}} = 9.38\rho_0 H^3$.

Off plane explosions: For an off plane explosion which occurs at z_{min} , the density ranges from $\rho(z_{\text{min}})$ to $\rho(z_{\text{max}} - z_{\text{min}})$, which the vertical scale increases from 0 to $z_{\text{max}} - z_{\text{min}}$. The resulting integral is

$$M_{\text{CSM}}(z_{\text{min}}, z_{\text{max}}) = 4\pi \int_0^{z_{\text{max}} - z_{\text{min}}} \rho(z + z_{\text{min}}) z^2 dz. \quad (\text{C3})$$

For the Gaussian profile we have

$$\begin{aligned} \frac{M_{\text{CSM}}}{4\pi\rho_0 H^3} &= \sqrt{\frac{\pi}{2}} (1 + \zeta_{\text{min}}^2) \left[\operatorname{erf}\left(\frac{\zeta_{\text{max}}}{\sqrt{2}}\right) - \operatorname{erf}\left(\frac{\zeta_{\text{min}}}{\sqrt{2}}\right) \right] \\ &\quad - e^{-\zeta_{\text{min}}^2/2} \zeta_{\text{min}} - e^{-\zeta_{\text{max}}^2/2} (\zeta_{\text{max}} - 2\zeta_{\text{min}}) \end{aligned} \quad (\text{C4})$$

where $\zeta_{\text{max/min}} = z_{\text{max/min}}/H$. For model 9 we use $\zeta_{\text{max}} = \infty$ and $\zeta_{\text{min}} = 1$, and the resulting mass is $M_{\text{CSM}} = 1.92M_{\odot}$. For model 10 we use $\zeta_{\text{max}} = \infty$ and $\zeta_{\text{min}} = 2$, and the resulting mass is $M_{\text{CSM}} = 0.15M_{\odot}$.

For the radiation dominated profile we have

$$\begin{aligned} \frac{M_{\text{CSM}}}{4\pi\rho_0 H^3} &= \int_{\zeta_{\text{min}}}^{\sqrt{6}} (\zeta - \zeta_{\text{min}})^2 \left(1 - \frac{\zeta^2}{6}\right)^3 d\zeta = \frac{\zeta_{\text{min}}^9}{54432} - \frac{\zeta_{\text{min}}^7}{1260} \\ &\quad + \frac{\zeta_{\text{min}}^5}{60} - \frac{\zeta_{\text{min}}^3}{3} + \frac{16\sqrt{6}\zeta_{\text{min}}^2}{35} - \frac{3\zeta_{\text{min}}}{2} + \frac{32\sqrt{2}}{35\sqrt{3}}. \end{aligned} \quad (\text{C5})$$

For model 11 we use $\zeta_{\text{min}} = 1$, and the resulting mass is $M_{\text{CSM}} = 0.49M_{\odot}$. For model 12 we use $\zeta_{\text{min}} = 2$, and the resulting mass is $M_{\text{CSM}} = 6.4 \cdot 10^{-4}M_{\odot}$.

APPENDIX D: LIGHTCURVE COMPUTATION IN THE 2D MODELS

We first define an observer plane placed above the disc, parallel to the disc plane. From behind the disc, we solve the simple radiative transfer equations along parallel lines of sight to obtain the intensity at each position on the observer plane by computing the sequence

$$I(z + \Delta z) = I(z) e^{-\Delta\tau} + S(1 - e^{-\Delta\tau}), \quad (\text{D1})$$

where I is the intensity, S is the source function and $\Delta\tau = \rho\kappa\Delta z$ is the optical depth along a small distance Δz . We assume black body radiation for the source function ($S = \sigma T^4/\pi$) and only compute the bolometric luminosity. For opacity, we only assume electron scattering ($\kappa = 0.2(1+X) \text{ cm}^2 \text{ g}^{-1}$, where X is the hydrogen fraction). We do not take into account the effect of recombination in order to avoid making the disc unreasonably optically thin due to the way we set the initial disc temperature. This choice should not affect the early evolution of the lightcurve, at least in the planar phase. The intensity is then integrated over the whole observer plane and multiplied by 4π to obtain the luminosity. We refer the reader to [Suzuki et al. \(2016\)](#) for more details of the idea behind the calculation procedure.

Because radiation transport is not coupled to the hydrodynamics in our 2D simulations, this methodology does not account for the diffusion and radiative cooling in the ejecta. Therefore, the lightcurves obtained this way may not be energetically self-consistent. Additionally, the temperature in the outer parts of the ejecta may be overestimated. If the outer parts of the ejecta have sufficiently cooled, the atoms may recombine and lower the opacity, affecting the later lightcurve. Nevertheless, this estimate should give us a rough idea of how the shock breakout may be observed.

This paper has been typeset from a $\text{\TeX}/\text{\LaTeX}$ file prepared by the author.